

## Hinode EIS: updated in-flight radiometric calibration

G. DEL ZANNA,<sup>1</sup> M. WEBERG,<sup>2</sup> AND H. P. WARREN<sup>3</sup>

<sup>1</sup>*DAMTP, Center for Mathematical Sciences, University of Cambridge, Wilberforce Road, Cambridge, CB3 0WA, UK*

<sup>2</sup>*Department of Physics and Astronomy, George Mason University, Fairfax, VA, USA*

<sup>3</sup>*Space Science Division, Naval Research Laboratory, Washington, DC 20375, USA*

Submitted to ApJ

### ABSTRACT

We present an update to the in-flight radiometric calibration of the Hinode EUV Imaging Spectrometer (EIS), revising and extending our previous studies. We analyze full-spectral EIS observations of quiet Sun and active regions from 2007 until 2022. Using CHIANTI version 10, we adjust the EIS relative effective areas for a selection of dates with emission measure analyses of off-limb quiet Sun. We find generally good agreement (within typically  $\pm 15\%$ ) between measured and expected line intensities. We then consider selected intensity ratios for all the dates and apply an automatic fitting method to adjust the relative effective areas. To constrain the absolute values from 2010 we force agreement between EIS and Solar Dynamics Observatory (SDO) Atmospheric Imaging Assembly (AIA) 193 Å observations. The resulting calibration, with an uncertainty of about  $\pm 20\%$ , is then validated in various ways, including flare line ratios from Fe XXIV and Fe XVII, emission measure analyses of cool active region loops, and several density-dependent line ratios.

*Keywords:* Solar extreme ultraviolet emission - The Sun - Calibration

### 1. INTRODUCTION

The Hinode Extreme Ultraviolet Imaging Spectrometer (EIS) (Culhane et al. 2007) has observed the solar corona in two wavelength bands regularly since 2006. These wavebands are commonly referred to as the shortwave (SW, 170–211 Å) and longwave (LW, 242–292 Å) channels. An accurate EIS relative calibration is necessary e.g. to measure electron densities (see, e.g. Young et al. 2009), to obtain estimates of emission measures (see, e.g. Warren et al. 2011), to measure electron temperatures and test for the presence of non-Maxwellian electron distributions via line ratios (see, e.g. the Del Zanna & Mason 2018, review), and for estimates of the coronal magnetic fields (see, e.g. Li et al. 2016). An accurate absolute calibration is necessary for e.g. a meaningful comparison with other instruments such as IRIS (Del Zanna et al. 2022).

One way to monitor the in-flight degradation is to measure well-known intensity ratios of lines that are insensitive to variations of densities and temperatures and compare them

to expected values. We can rely on the accuracy of the atomic data for the strongest lines, after a series of scattering calculations and benchmark studies have dramatically improved the EIS spectral region. Significant improvements for the iron coronal lines observed by EIS came with the atomic data in CHIANTI version 8 (Del Zanna et al. 2015), with a few updates included in CHIANTI v.10 (Del Zanna et al. 2020). Typically, there is agreement between well-calibrated radiances of strong lines and the predicted ones within 10% or so.

One method to obtain the relative calibration is to use only spectral lines from the same ion, while another one is to use lines from ions formed at similar temperatures. Clearly, the first method is more robust as does not depend significantly on the plasma conditions and on uncertainties in the ionization fractions. This was used by Del Zanna (2013a), where a significant revision of the ground calibration was presented. In addition, a time-dependent decrease in the sensitivity of the LW channel was introduced, increasing the calibrated intensities of the LW lines by nearly a factor of two for data after 2008. Only data from 2006 until Sept 2012 were analysed. Still, deviations in several line ratios were present, indicating

the need for wavelength-dependent corrections within each EIS channel.

Such corrections were introduced by Warren et al. (2014), where observations of coronal lines during the 2006–2014 period were analysed. In this case, the second method was adopted: off-limb quiet Sun (QS) observations were selected, and assuming isothermality, the emission measure loci method was used to enforce agreement between observed and predicted intensities using a range of ions. This was repeated for several dates, to obtain a time- and wavelength-dependent revision of the ground calibration.

In the present paper, we extend our previous two studies in several ways. First, we analyse a wide range of observations covering the entire period until 2022, of the quiet Sun and active regions (AR), both on-disk and off-limb. Second, we relax the isothermal assumption and perform an emission measure analysis on off-limb QS to obtain a relative calibration for a sample of dates. Third, we extend the line ratio analysis of Del Zanna (2013a), including well-known ratios in QS, AR and perform an automatic best-fitting method to obtain the relative calibration amongst all wavelengths. Fourth, we constrain the absolute EIS calibration by comparing SW data to Solar Dynamics Observatory (SDO) Atmospheric Imaging Assembly (AIA, Lemen et al. 2012) 193 Å observations from 2010. Finally, we have run several checks that the calibration provides good agreement within  $\pm 20\%$  for a sample of flare observations, analysing Fe XXIV and Fe XVII lines, for cool lines that are present in AR loops, and for the density-sensitive lines.

Section 2 outlines the methodology adopted, while Section 3 describes the associated selection of the observations and data analysis. Section 4 describes a selection of the observations analysed here, while Section 5 draws the conclusions. An Appendix provides a few more examples among the data analysed.

## 2. METHODS

The results of our previous studies, and a preliminary analysis of further observations, clearly indicated strong wavelength-dependent variations in the EIS responsivity. The line ratio analysis adopted for EIS by Del Zanna (2013a) did not sufficiently sample the entire spectral region, considering separately the coronal 1–2 MK lines visible in the QS and the hotter 2–3 MK lines only visible in AR spectra. The additional step was to perform a DEM analysis.

### 2.1. DEM analysis on near-isothermal spectra

We adopted the method of selecting first off-limb QS observations, far enough from the limb to reduce the blending of cool lines, but close enough to retain enough counts. The advantage is that the plasma is nearly isothermal and isodensity in these cases. This is an extension of the method

used by Warren et al. (2014), as we relax the isothermality assumption and perform a differential emission measure (DEM) analysis. This method is more reliable than the line ratio method, as several line ratios, especially those involving lines far apart in wavelength, are somewhat temperature-dependent. Indeed several ratios of lines from the same ion have now been identified and can be used to measure the electron temperature (cf. Del Zanna & Mason 2018, and references therein).

The strongest lines in these off-limb spectra are from Fe IX–Fe XIII and Si X. First, we estimate the average electron density from the Si X 258 vs. 261 Å ratio. The Fe XIII 202.0, 203.8 Å and other line ratios have also been considered, but the Si X was deemed the best case for these QS observations as these lines are close in wavelength and the uncertainty in the relative calibration does not affect much the results. We then calculate the  $G(T)$  of all the lines possibly contributing to the observed EIS lines, assuming a constant density. We then perform a DEM analysis using a modified version of the CHIANTI v.10 DEM method, which defines the DEM as a spline function, and uses a nonlinear, least squares levenberg—marquardt fitting algorithm (MPFIT, Markwardt 2009).

We started with calibrated intensities using the ground calibration and aimed to obtain a correction to it, by defining a set of spline nodes for the corrections across the EIS spectral range, most of which are located where the strong lines are. The corrections were adjusted for each observation to obtain a good agreement between observed and predicted intensities. The DEM was obtained from a minimal list of lines from iron.

We then checked that the calibration obtained in this way produced good agreement between predicted and measured intensities of a few cooler lines formed below 1 MK. We selected a few AR loop regions, where the signal from the hotter lines was reduced, and performed a DEM analysis. Also in this case it is well known that the plasma distribution is nearly isothermal, which simplifies the modelling.

Clearly, we cannot expect for all lines agreement to say 10%, as departures from the isodensity case, optical depth and other effects can affect the results. Also, the atomic data for different ions do not have the same accuracy. However, what is important is the fact that those lines we have selected, for which good agreement between observed and predicted radiances is present, should have the same agreement regardless of the time of the observation.

### 2.2. Line ratios

The DEM analysis provides wavelength-dependent corrections to the ground calibration for a set of dates. Unfortunately, however, the DEM analysis is time consuming and it is not feasible to apply this method to all EIS observations.

To obtain a correction for any given date we fit the effective areas using a list of 39 line intensity ratios that are largely density-insensitive at typical AR and QS temperatures. The chosen ratios are listed in Table 4.

The general fitting methodology is as follows. First, we select a dataset of 79 AR and 88 QS observations that are relatively quiet and free of transient features. This dataset is an extension of the observations considered in [Del Zanna \(2013a\)](#). Next, we use the DEM analysis as anchor points and perform linear interpolation to estimate the EIS effective area curve at each observation time and compute the line ratios. Next, we produce a combined set of measured AR and QS line ratios by averaging, separately, all AR and QS observations within a six-month window and then concatenating the two lists together. Then, we fit the EIS effective area curve using MPFIT such that the relative errors of the line ratios are minimized when compared to the theoretical values. As an additional constraint, we also simultaneously minimize the relative ratios of select pairs of density-sensitive line ratios for Fe XII, Fe XIII, Fe XIV, & Si X. Since only the relative ratio of each pair of density-sensitive ratios is used in the minimization, the actual density value computed from each individual line ratio can be ignored.

### 2.3. Emissivity ratios

As EIS data are often used to measure electron densities via line ratios, we have included various checks to make sure that the results have some consistency. Generally, one expects densities obtained by ions formed at similar temperatures to be similar. Also, that densities obtained from lines within the same ion are consistent, although in principle some differences could occur if the plasma is strongly non-uniformly distributed. Significant discrepancies within the Fe XII lines and in the densities obtained by Fe XII and Fe XIII have been reported in the literature, see e.g. [Young et al. \(2009\)](#).

One way to assess at once all the line ratios within an ion is to plot the emissivity ratios ([Del Zanna et al. 2004](#)), which are obtained by dividing the observed intensity  $I_{ob}$  of a line by its emissivity

$$F_{ji} = \frac{I_{ob} N_e C}{N_j(N_e, T_e) A_{ji}} \quad , \quad (1)$$

calculated at a fixed electron temperature  $T_e$  and plotted as a function of the density  $N_e$  ( $N_j$  is the population of the upper state, and  $A_{ji}$  the transition rate for spontaneous emission). This method works if the lines have a similar temperature dependence. If the plasma is uniformly distributed along the line of sight, the curves should form a crossing, which indicates the averaged density. The scaling constant  $C$  is arbitrarily chosen so that the crossing occurs at a value around 1.

We have applied the emissivity ratios to selected observations of Fe XII, Fe XIII, and Si X over the years. As these ions are formed at similar temperatures, we expect the densities to be similar. When the emissivities of the lines are independent of density, as in the case of the Fe XVII lines, the emissivity ratios are plotted as a function of temperature.

### 2.4. Opacity in coronal lines and other effects

The strongest EIS SW lines in the quiet Sun are three decays to the ground state, from  $^4P$  states, at 192.4, 193.5, and 195.1 Å. The latter line is a self-blend with a weak density-sensitive transition ([Del Zanna & Mason 2005](#)), which only contributes a few percent for very high densities. The intensity ratios of the 192.4, 193.5, and 195.1 Å lines are not sensitive to density or temperature.

An analysis of hundreds of EIS observations of different features, on-disk, off-limb, with different exposures, slit combinations found several anomalies in the 192.4, 193.5, and 195.1 Å lines ([Del Zanna et al. 2019](#)). The main ones affect the instrumental widths of the 193.5, and 195.1 Å lines, which are anomalous, and reduced intensities of the same lines (compared to the weaker 192.4 Å), in all on-disk active region and many off-limb observations. The 195 Å line is typically weaker than expected by 30–40 %. Note that the intensity of the 195.1 Å line should actually increase in active region observations, due to the presence of the above-mentioned self-blend, and not decrease. The only explanation found for the anomalous ratios of these lines was that optical depth effects are ubiquitous.

The intensity ratios of the 192.4, 193.5, and 195.1 Å lines in on-disk QS observations are stable and have been used to constrain the relative calibration between these wavelengths. There are a few other strong decays to the ground states of other ions, with large oscillator strengths, however establishing opacity in these other cases is non-trivial. For this reasons, we rely more on the line ratios of the on-disk QS observations to assess the validity of our revised calibration.

We have also preferred active region observations off-limb, and selected areas away from the bright moss regions, to reduce possible effects in some line ratios due to non-Maxwellian electron distributions (NMED). In fact, some evidence based on EIS and IRIS observations have indicated that NMED are present in active regions ([Lörinčik et al. 2020](#); [Del Zanna et al. 2022](#)).

### 2.5. Absolute calibration

Obtaining an absolute calibration is notoriously difficult. [Del Zanna \(2013a\)](#) noted that using the ground calibration, where a few wavelengths were calibrated against laboratory standards, the radiances of the SW lines in the QS were close to previously measured values, for observations in 2006–2007. This indicated that the ground calibration was relatively accurate for the SW channel. One problem with that

comparison was the paucity of previous radiance observations, and significant solar variability. Also, most previous measurements were of the Sun as a star, and the irradiances had to be converted to radiances.

Another indication that the SW ground calibration was correct in 2010 came with direct comparisons of EIS SW vs. SDO AIA 193 Å observations, as e.g. described in [Del Zanna et al. \(2011\)](#); [Del Zanna \(2013b\)](#). As the SW observes the main wavelengths contributing that AIA band, it is in principle straightforward to cross-calibrate the entire SW channel against AIA, after taking into account the different spatio-temporal resolutions, and carefully removing the EIS bias. The AIA 193 Å calibration was checked summing the signal from the full Sun and comparing it against the predicted values from the SDO EVE irradiances.

In turn, the EVE calibration relies on a comparison with a few sounding rocket flights and adjustments using line ratios, following the methods adopted for EIS ([Del Zanna 2013a](#)). The prototype EVE flown on the sounding rocket flights is regularly calibrated on the ground. The absolute calibration of the EVE prototype is deemed accurate to within 20%, although detailed comparisons carried out on the first flight in 2008 showed larger discrepancies (40%) for some among the strongest lines ([Del Zanna & Andretta 2015](#); [Del Zanna 2019](#)). Calibration flights were obtained in 2011, 2012, 2013, 2018, 2021 plus a recent one in 2023.

The failure of EVE MEGS-A in 2014 meant that no direct AIA/EVE cross-calibrations could be carried out after that date. After 2014, the only useful cross-calibration EVE sounding rockets were flown in 2018, 2021, and 2023. The decrease in the sensitivity of the AIA 193 Å band has been linearly interpolated between 2014 and 2018, which brings some additional uncertainty. The calibration of the recent flights is still ongoing.

Any cross-calibration is never straightforward, especially when considering broad-band observations such as the AIA ones, as a wavelength-dependent degradation would affect the results. Such degradation is very common in space, and indeed has been measured by EVE using different filters. Fortunately, the overall count rates in the AIA 193 Å band only show a decrease of about 10% over the first four years, when compared to EVE data. This indicates moderate degradation, and confirms that this band is usable for the EIS calibration.

Here, we used a set of co-temporal and co-spatial EIS/AIA observations to constrain the EIS SW overall absolute calibration, adopting our revised time- and wavelength-dependent EIS calibration. We used the modelled AIA degradation as available in SolarSoft, with the option of the normalisation with SDO EVE (keyword *evenorm*). We also checked this AIA calibration against a few simultaneous SDO EVE observations, using the latest EVE calibration,

finding agreement to within a few percent. After the fitting the new effective area curves using the method described in section 2.2, we scale the absolute values of both EIS channels such that the total integrated effective area in the fit SW channel matches that of ground calibrated SW channel after correcting for the observed declining trend of the EIS / AIA 193 Å ratio after 2010. No scaling was applied to fit effective areas before 2010.

### 3. DATA ANALYSIS AND SELECTION OF THE OBSERVATIONS

The EIS data used to obtain the relative calibration were processed with custom-written software (see, e.g. [Del Zanna et al. 2011](#)). The hot, warm and dusty pixels are flagged as missing, following the database available via SolarSoft. Unfortunately, the number of residual warm pixels not flagged has increased significantly in data during the past few years. The location of the residual warm pixels is also variable. We have tried to avoid the most affected regions in each EIS raster, selecting areas with visual inspection. However, the weakest lines after 2018 are significantly compromised by the presence of these warm pixels, which have the effect of increasing their intensities.

The pixels affected by particle events are also flagged as ‘missing’. We used the routine *new\_spike*. All the missing pixels are then replaced with interpolated values with a series of interpolations along different directions. The exposures are then visually inspected.

The full spectral atlases are rotated to remove the slant in the spectra, and the two SW and LW channels aligned, taking into account the different displacements over time.

As the dark frames (bias) are extremely variable and unknown, a base minimum value is removed from each exposure. Total data numbers (DN) in the lines are obtained with Gaussian fitting and a polynomial background. The background and line fitting is obtained over different spectral ranges. We note that the bias is very difficult to estimate in the central part of the SW channel. Different choices for the background can affect the weakest lines by a few percent. EIS saturation is near 16000 DN, however we found indications of some non-linear effects for lower values ([Del Zanna et al. 2019](#)), so we have avoided areas near saturation.

## 4. RESULTS

### 4.1. QS off-limb DEM analysis

Table 1 lists the selection of coronal lines and the results of the DEM for the QS off-limb observation on 11 Mar 2007. Only a few lines from iron, as listed in the Table, were used for the DEM, so the results are independent of chemical abundance issues. The resulting DEM is shown in Fig. 1. The points for all the coronal lines are plotted at the temper-

ature  $T_{\max}$  where the line contribution function  $G(T)$  has a maximum. In the ordinate, we plot the ratio of the theoretical vs. the observed intensity multiplied by the DEM value at that temperature, to provide a visual indication of which main lines constrain the DEM, and how close the predicted radiances are to the observed ones. The peak of the DEM is close to  $\log T$  [K] = 6.15, typical of the QS near the limb, but the distribution is not strictly isothermal. Nevertheless, most of the strongest lines are formed at this temperature, which makes the comparison between lines from different ions much easier. This can be seen in Table 1 where  $T_{\max}$ , as well as the effective temperature  $T_{\text{eff}}$ :

$$T_{\text{eff}} = \int G(T) DEM(T) T dT / \int G(T) DEM(T) dT \quad , \quad (2)$$

are listed.  $T_{\text{eff}}$  is an average temperature more indicative of where a line is formed. The Table also shows the total counts in each line and the calibrated radiance obtained with the present calibration.  $R$  is the ratio between the predicted and observed radiances. We can see that generally all lines are well reproduced within  $\pm 15\%$ , but examining lines from the same ion, relative differences are generally within  $\pm 5\%$ .

Also note that the list includes lines that are strongly density dependent, indicating that the isodensity approximation is relatively accurate. To calculate the line emissivities we used a constant electron density of  $2 \times 10^8 \text{ cm}^{-3}$ . The few Si X lines in the LW channel are also very useful to constrain the LW sensitivity. Typically, the silicon abundance variations are in line with those of iron, so again the results are virtually independent of the chemical abundances.

A few of the extremely weak lines, with total data numbers below 100 are not well reproduced. That is of no concern. The intensity ratios of the 192.4, 193.5, and 195.1 Å lines indicate some opacity effects.

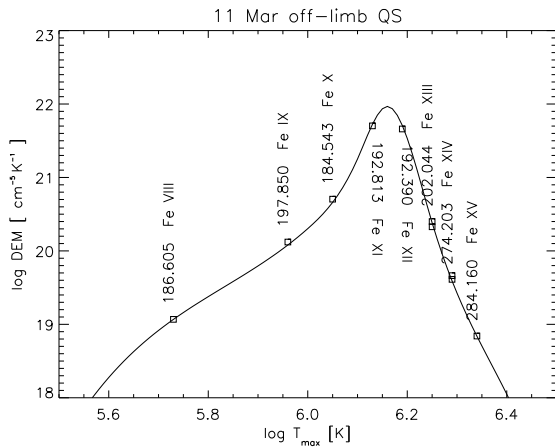


**Figure 1.** DEM for the QS off-limb on 11 Mar 2007. The points are plotted at the temperature  $T_{\max}$ , and at the theoretical vs. the observed intensity ratio multiplied by the DEM value.

**Table 1.** QS off-limb observation on 11 Mar 2007 (90 s, 1'' slit).  $\lambda_{\text{obs}}$  and  $\lambda_{\text{exp}}$  (Å) are the observed and CHIANTI wavelengths, DN are total counts,  $I_{\text{obs}}$  is the radiance ( $\text{phot cm}^{-2} \text{ s}^{-1} \text{ arc-second}^{-2}$ ).  $T_{\max}$  and  $T_{\text{eff}}$  are the maximum and effective temperature (log values, in K; see text),  $R$  the ratio between predicted and observed radiances, and  $r$  the fractional contribution to the blend. The lines used for the DEM have a \* while those density-dependent have a dd.

$\lambda_{\text{obs}}$	DN	$I_{\text{obs}}$	$\log T_{\max}$	$\log T_{\text{eff}}$	$R$	Ion	$\lambda_{\text{exp}}$	$r$
194.66	90	1.2	5.72	6.08	0.72	Fe VIII	194.661	0.92
185.22	61	4.0	5.73	6.08	1.02	Fe VIII	185.213	0.94
* 186.60	70	3.3	5.73	6.08	1.00	Fe VIII	186.598	0.83
189.94	155	3.9	5.94	6.12	0.91	Fe IX	189.935	0.95
188.49	247	8.2	5.95	6.12	0.93	Fe IX	188.493	0.89
* 197.85	268	4.6	5.96	6.13	0.91	Fe IX	197.854	0.93
257.26	464	54.7	6.04	6.14	0.89	Fe X	257.259	0.21
						Fe X	257.263	0.76
177.24	87	101.1	6.05	6.14	1.05	Fe X	177.240	0.97
174.53	53	179.2	6.05	6.14	1.03	Fe X	174.531	0.98
* 184.54	580	45.4	6.05	6.14	0.90	Fe X	184.537	0.96
dd 190.04	728	18.2	6.06	6.15	1.03	Fe XII	190.040	0.17
						Fe X	190.037	0.71
257.55	142	16.4	6.12	6.15	1.15	Fe XI	257.554	0.70
						Fe XI	257.547	0.26
256.92	233	28.2	6.12	6.15	0.86	Fe XI	256.919	0.91
dd 182.17	178	30.0	6.13	6.16	1.02	Fe XI	182.167	0.97
188.30	1920	66.1	6.13	6.16	1.07	Fe XI	188.299	0.97
188.22	3110	108.8	6.13	6.16	1.06	Fe XI	188.216	0.97
* 192.81	1440	23.7	6.13	6.16	1.05	Fe XI	192.813	0.96
180.40	608	194.2	6.13	6.16	1.19	Fe XI	180.401	0.97
dd 202.71	141	9.3	6.13	6.16	1.14	Fe XI	202.705	0.94
253.79	72	11.3	6.15	6.16	0.90	Si X	253.790	0.97
dd 258.37	536	58.7	6.15	6.16	0.90	Si X	258.374	0.97
dd 271.99	475	30.4	6.15	6.16	0.89	Si X	271.992	0.97
dd 261.06	375	34.6	6.15	6.16	0.90	Si X	261.056	0.98
dd 277.27	273	23.5	6.15	6.16	0.89	Si X	277.264	0.98
dd 256.40	435	54.8	6.16	6.16	1.07	Si X	256.377	0.63
						Fe XII	256.410	0.18
dd 196.64	491	7.4	6.19	6.16	1.17	Fe XII	196.640	0.93
dd 186.88	610	27.3	6.19	6.16	1.09	Fe XII	186.854	0.16
						Fe XII	186.887	0.77
dd 203.73	132	12.3	6.19	6.17	0.79	Fe XII	203.728	0.96
193.51	6640	99.5	6.19	6.17	1.23	Fe XII	193.509	0.95
* 192.39	2860	50.5	6.19	6.17	1.12	Fe XII	192.394	0.96
195.12	10300	136.0	6.19	6.17	1.31	Fe XII	195.119	0.97
dd 196.52	170	2.5	6.24	6.17	0.99	Fe XIII	196.525	0.89
dd 200.02	303	7.6	6.24	6.17	0.77	Fe XIII	200.021	0.94
dd 261.73	40	3.6	6.25	6.18	1.10	Fe XIII	261.743	0.97
dd 203.83	243	23.3	6.25	6.18	1.12	Fe XIII	203.795	0.28
						Fe XIII	203.826	0.62
dd 246.21	50	15.6	6.25	6.18	1.03	Fe XIII	246.209	0.95
* 251.95	144	26.7	6.25	6.18	1.13	Fe XIII	251.952	0.97
dd 204.94	57	7.4	6.25	6.18	0.88	Fe XIII	204.942	0.96
209.92	51	18.6	6.25	6.18	0.97	Fe XIII	209.916	0.96
* 202.04	2040	103.0	6.25	6.18	0.96	Fe XIII	202.044	0.97
dd 264.79	296	24.2	6.29	6.18	0.89	Fe XIV	264.789	0.67
						Fe XI	264.772	0.30
* 274.20	349	24.2	6.29	6.19	0.96	Fe XIV	274.204	0.95
252.20	19	3.5	6.29	6.19	1.01	Fe XIV	252.200	0.94
dd 257.40	55	6.5	6.29	6.19	1.05	Fe XIV	257.394	0.96
dd 270.52	128	9.4	6.29	6.19	1.06	Fe XIV	270.521	0.97
* 211.32	80	37.1	6.29	6.19	0.85	Fe XIV	211.317	0.96
* 284.16	169	31.3	6.34	6.20	1.00	Fe XV	284.163	0.96

The other observations were processed in a similar way, and the results are provided in the Appendix. Generally, the consistency between observed and predicted radiances is the same, indicating that for those observations, the accuracy of the relative sensitivity at specific wavelengths is within  $\pm 15\%$ . We used the set of effective areas obtained in this way as a baseline when using the line ratios as shown below.

#### 4.2. On-disk AR loop DEM analysis

Several low- $T$  lines become prominent in AR loops, and they are useful to cross-check the relative calibration at wavelengths different than those of the coronal lines. AR loop legs are nearly isodensity and isothermal (cf Del Zanna & Mason 2018, and references therein) so they are also good sources for the cross-calibration.

As we are not interested in the coronal lines in this case, only the cooler lines are considered to check the relative calibration. As multiple isothermal structures are present in AR cores (cf Del Zanna 2013b), obtaining a DEM which reproduces well all lines is challenging, compared to the QS off-limb case. Nevertheless, as we are primarily concerned to check the relative agreement between lines from the same ion or lines with similar effective temperatures, an accurate estimate of the DEM is not necessary.

We have performed the analysis on a few cool loops at different dates, and found general consistency using the effective areas obtained with the previous method. One example is provided in the Appendix.

#### 4.3. Line radiances

The large solar variability precludes the use of QS radiances for the EIS calibration, as carried out for the SOHO CDS, as only two low-temperature lines are available, the He II 256.3 Å and the O V 192.9 Å. The former is blended with several coronal lines, and the latter is weak and hard to measure. However, several transition-region lines are expected to show a small variation with the solar cycle, and should have similar radiances during the 2008 and 2019 minima. Fig. 2 (top) shows the count rates in two cool SW lines. It is clear that there is a decrease in the signal, especially after 2010. Fig. 2 (bottom) shows the corrected radiances with the present calibration.

Fig. 3 (top) shows the count rates in the He II 256.3 Å, which has been deblended from its coronal contributions, and a weak Mg VII line. The signal in the He II line during 2007 was relatively constant, but then had a significant drop in 2010, with a subsequent constant behaviour. On the other hand, all the lines at longer wavelengths show a very different behaviour: a nearly constant one until 2010, followed by a drop until 2016. This is a clear indication of a very different decrease in sensitivity at different wavelengths, which is difficult to explain and account for.

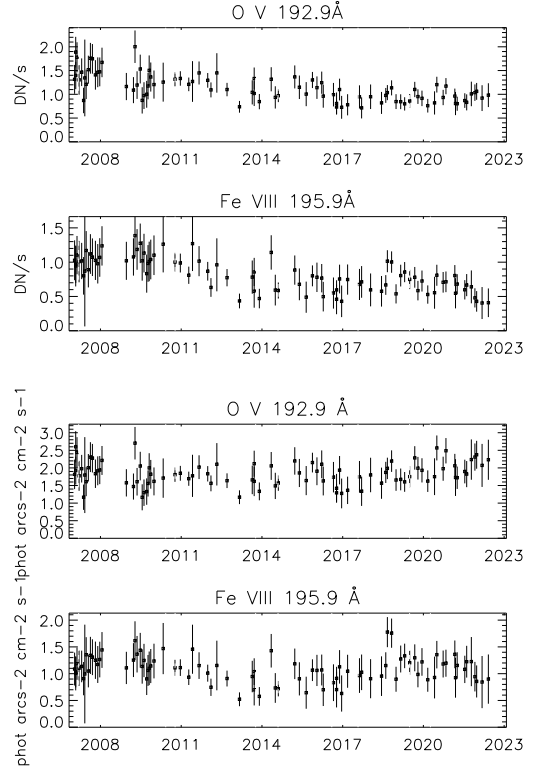


**Figure 2.** Top: Hinode EIS quiet Sun count rates (DN/s) in two cooler SW lines. Bottom: radiances with the present calibration.

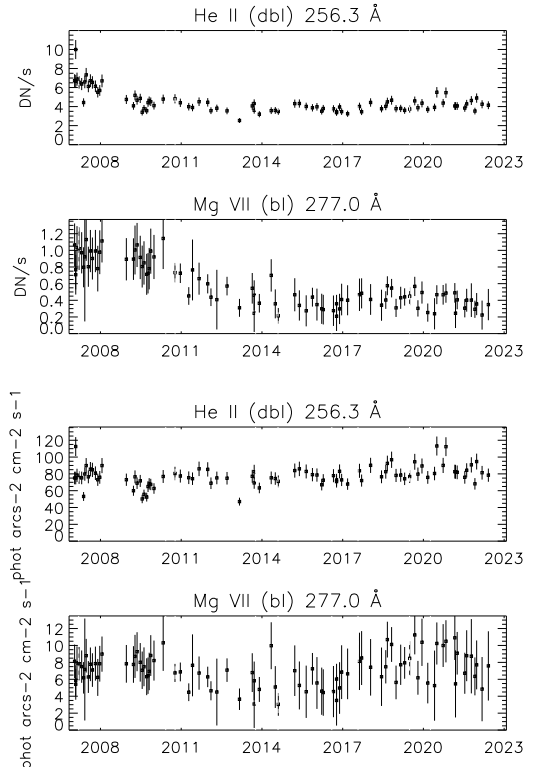


**Figure 3.** Top: Hinode EIS quiet Sun count rates in two cooler LW lines. Bottom: radiances with the present calibration.

#### 4.4. Line ratios

We extended the analysis of the dataset considered in [Del Zanna \(2013a\)](#), i.e. a set of on-disk QS regions, and a set of AR observations, mostly off-limb to reduce the contamination of the coronal lines from the cooler lines and opacity effects. For each observation, suitable regions were selected to obtain averaged spectra, and all lines fitted.

We selected several known ratios which are expected to be rather constant. They are listed in the Appendix. Most of the ratios are the same used in [Del Zanna \(2013a\)](#). Only a limited number of line ratios are well measured in on-disk QS regions. Lines formed above 1.5 MK such as Fe XIII are only well observed in AR observations.

Figures 4 and 5 show example fit effective areas for two different ARs observed, respectively, in 2011 and 2019. The left column of each figure contain the SW effective areas while the right column contain the LW. The top two panels in both columns show the relative line ratios of the pre-flight (top) and fit (middle) effective area profiles. A relative ratio of 1 indicates a perfect match with the theoretical line ratio. In both AR, the fit profiles greatly improve the relative ratios. Compared to the pre-flight profiles, the fit effective areas exhibit finer-scaled variations and have notable "shoulders" in both the SW (around 197 – 200 Å) and LW (265 – 269 Å) bands. The LW profiles shows more significant degradation over time than the SW profiles. It is worth noting here that the shape of the fit effective area profiles is sensitive to the number and spacing of the spline knots using for the fitting process. More knots allow for a better fit to each individual time period but also results in "wavy" profiles with more local maxima and minima and year-to-year variation of shapes. On the other hand, fewer spline knots results in smoother profiles but lower quality fits. Since we do not know the primary cause of the decline in EIS sensitivity, we do not have any reason to bias the fit towards wavy or smooth profiles. Therefore, after experimenting with a variety of spline knot spacings, we settled on using an average spacing of 5 Å between spline knots in both the SW and LW bands, with one knot removed from 170 Å, in the tail of the SW profile, and two extra knots added at 192.5 and 197.5 Å, near the SW peak. This resulted in profiles that were moderately smooth, yet still fit the observed line ratios well. Altogether, we used 20 spine knots to perform the fitting, which is a moderate increase over the 14 spline knots used for the fitting in [Warren et al. \(2014\)](#). The spline knots used for the preliminary DEM analysis of the off-limb data are slightly more irregular (cf. the Appendix).

Figures 6 and 7 compare selected line ratios computed over time using the pre-flight (black diamonds) and fit (blue crosses) effective areas. The ratios were normalized by their respective theoretical values. In both figures, the left two columns contain lines in the SW channel, the right two

columns show ratios in the LW channel, and the middle column contains cross-channel ratios. Most of the fit line ratios show dramatic improvement over the pre-flight ratios, with new values falling within 20% of the theoretical values. However, a few ratios show little to no improvement.

#### 4.5. Flare observations: Fe XXIV and Fe XVII

A few lines become prominent in flare observations and offer the possibility to check the relative calibration at different wavelengths. As only a few flares have been observed by EIS with a sufficient number of lines, the check is rather limited. The best ions are Fe XXIV and Fe XVII.

The Fe XXIV 192/255 Å is a good ratio to validate the SW/LW cross-calibration, as it does not depend on density or temperature, and could only be affected by H, He absorption or opacity effects. The lines are usually blended with several transitions (e.g. [Del Zanna 2008](#)), but for strong flares the Fe XXIV is dominant. We have computed the Fe XXIV 192 and 255 Å intensities for all available EIS `FlareResponse` and `HH_Flare` rasters and manually selected observations where the flare produced more than 50 pixels with statistically significant intensities, but were not dominated by pixels with saturation or diffracted signal. As is seen in Figure 8, when using the ground calibration the ratio departs by more than 50% from the expected value. The few data points between 2015 and 2018 also indicate a trend for the ratio to decrease. Using the updated calibration described in this paper brings the ratios to agreement with theory to within  $\pm 20\%$ .

As reviewed by [Del Zanna & Ishikawa \(2009\)](#), Fe XVII produces several lines in the EIS channels. The 204.6 and 254.9 Å form a branching ratio, for which atomic data are very accurate, and therefore are useful to validate the SW/LW cross-calibration. Many other Fe XVII lines are available across the LW channel, although they become usable and unblended only in larger flares. The line ratios do not have any density dependence and negligible temperature dependence, hence are excellent for the calibration.

Figure 9 shows the emissivity ratio curves relative to the main Fe XVII lines observed by Hinode EIS on two M2-class flares. With the exception of the very weak lines at 259.59 and 288.95 Å, all the line emissivities agree within  $\pm 20\%$ .

#### 4.6. Absolute calibration after 2010: EIS vs. AIA

The absolute values for the EIS responsivity have been constrained by a direct comparison between the EIS SW and the AIA 193 Å count rates using several observations after 2010. We gave preference to active region observations to have a better signal in the EIS spectra. The 'bias' in the EIS spectra has been fitted pixel-by-pixel on the spectra in DN. To predict the AIA DN/s we have used the AIA effective areas obtained using the `/evenorm` and `/time` dependent

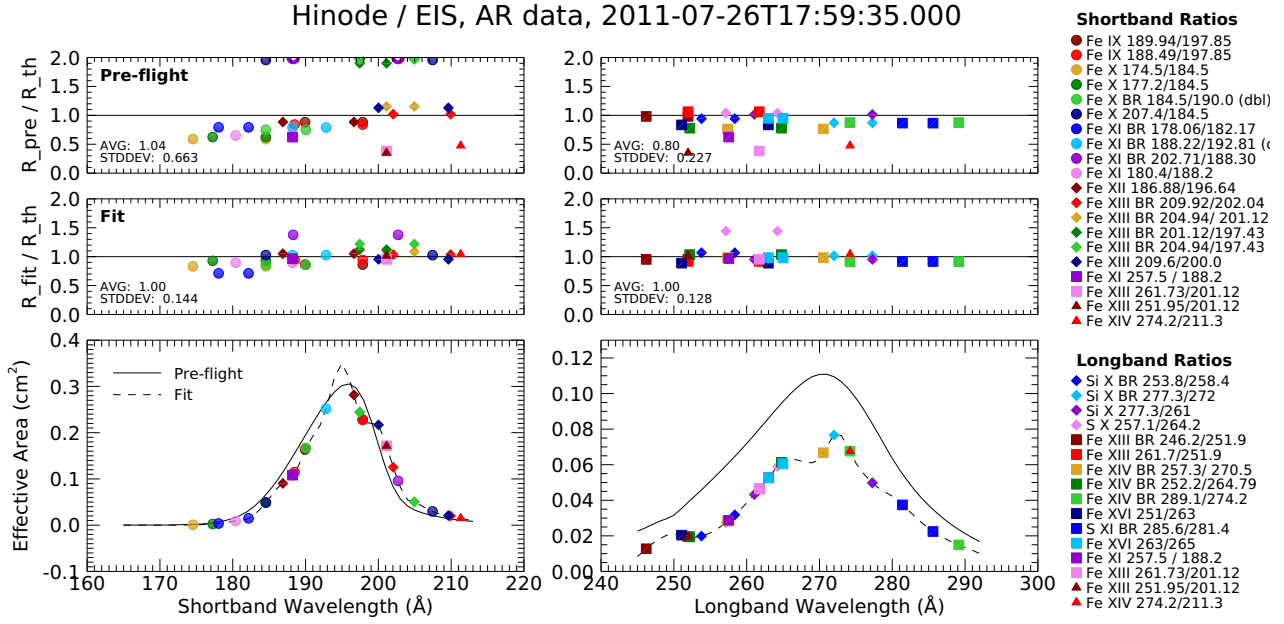


Figure 4. Example fit effective area curves for an active region observed on 2011-07-26.

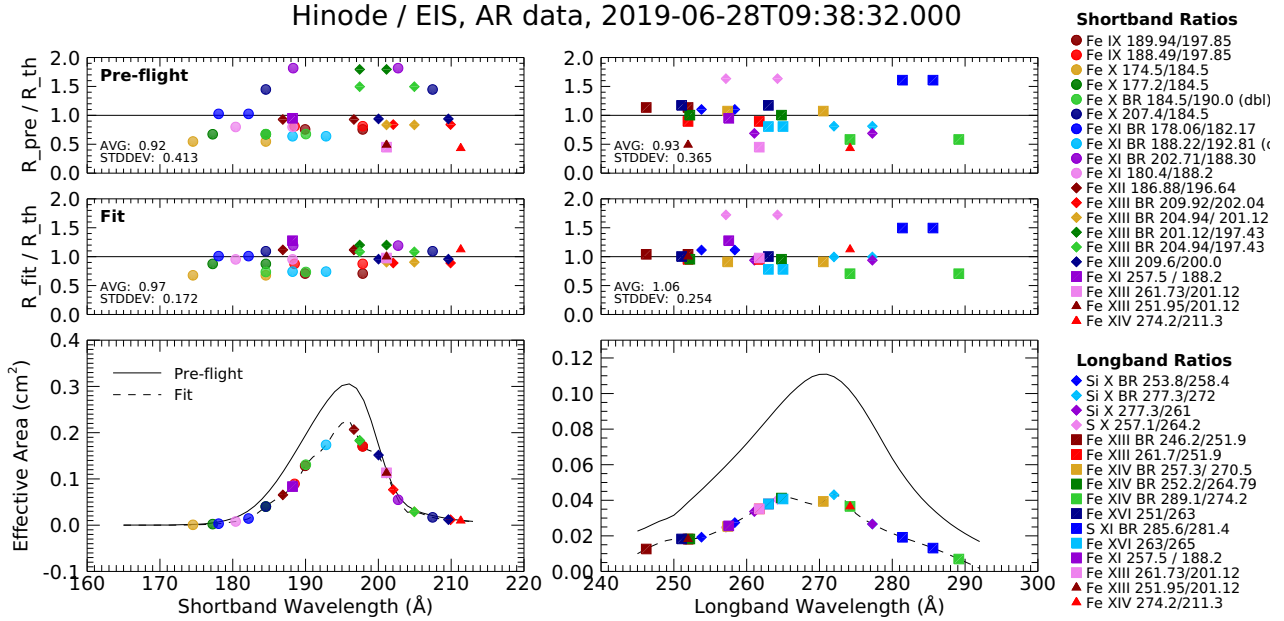
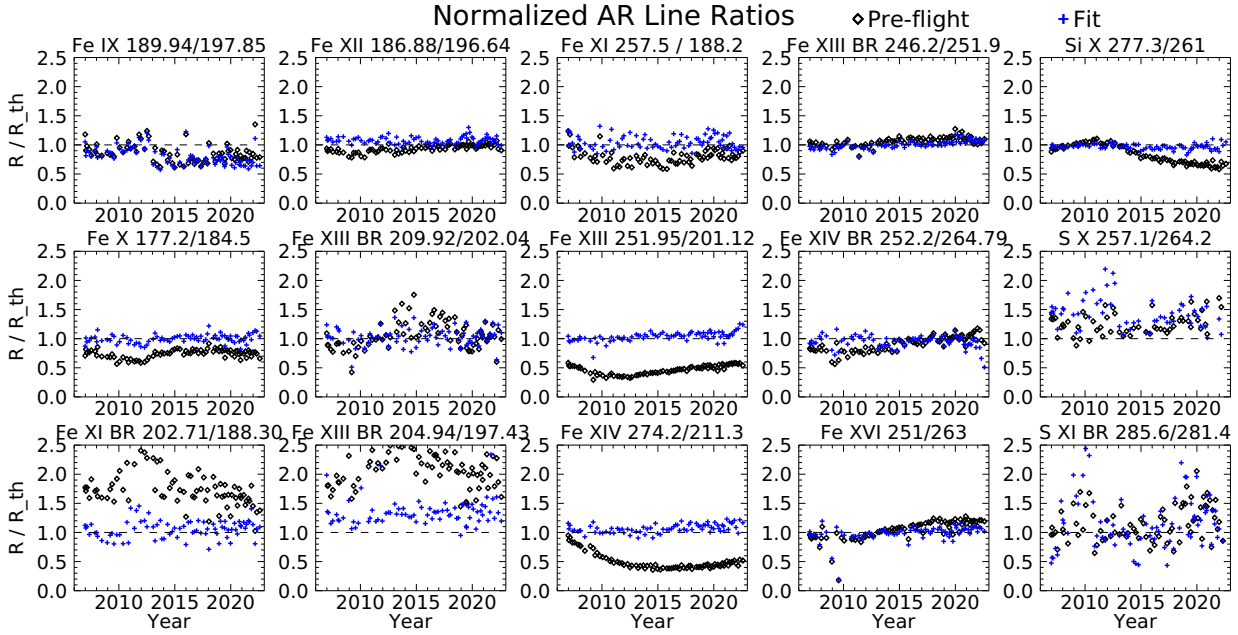


Figure 5. Example fit effective area curves for an active region observed later in the mission on 2019-06-28.

keywords. The AIA data have been resampled to the temporal and spatial resolution of EIS. On a pixel-by-pixel basis, there is generally a large scatter of values, partly due to the different point spread functions (PSF) of the instruments, and the lack of exact simultaneity in the observations. Nevertheless, averaging over spatial areas reduces the scatter, so the relative calibration can be estimated with only a few percent accuracy. More details are provided in the Appendix.

The averaged ratio between predicted and measured AIA DN obtained using the EIS ground calibration indicates a degradation of nearly a factor of two, as shown in Fig. 10 (top). This is clearly due to a decrease in the sensitivity of the EIS SW channel with time.

To obtain the EIS absolute calibration, we have first used the revised EIS SW relative calibration obtained with the previous methods to obtain calibrated units, to then convert them to predicted AIA counts. We have then applied corrections



**Figure 6.** Relative line ratios observed in AR over time. Ratios computed using the pre-flight calibration are shown as black diamonds and ratios computed from the new fits are shown as blue crosses.

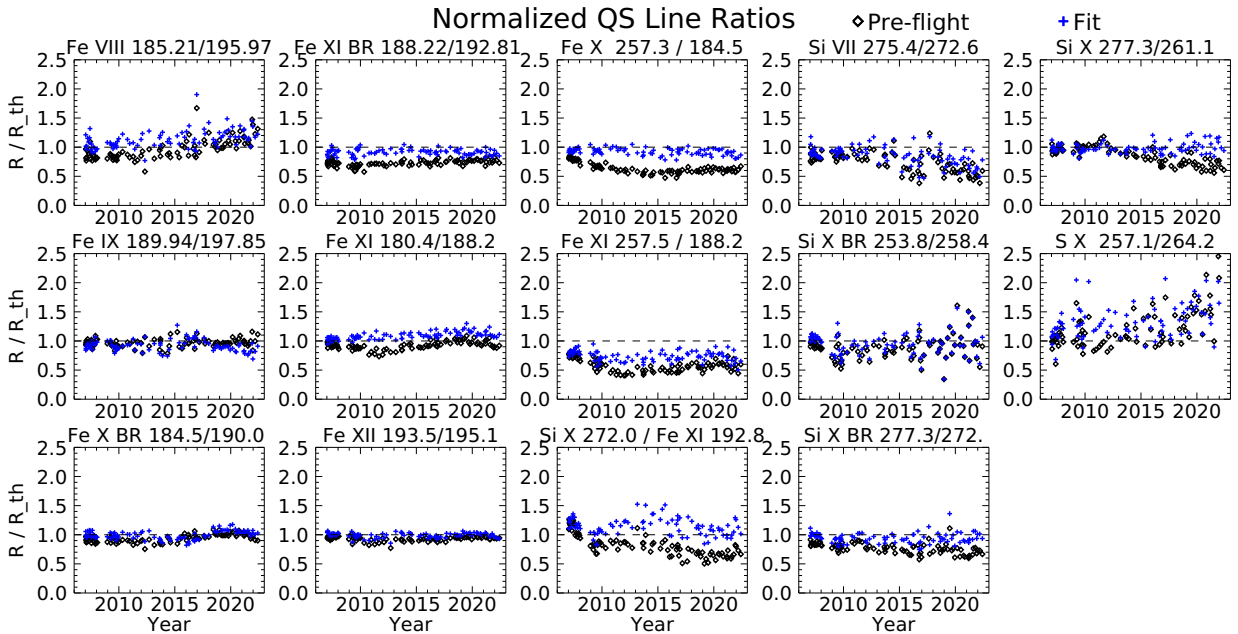


**Figure 7.** Relative line ratios observed in QS over time. Ratios computed using the pre-flight calibration are shown as black diamonds and ratios computed from the new fits are shown as blue crosses.

factors to the grid of selected dates, to obtain a better match with AIA. The results are shown in Fig. 10 (bottom).

#### 4.7. Absolute calibration before 2010

Establishing the absolute calibration before 2010 is difficult. We would normally expect the sensitivity at all wavelengths to decrease with time, hence the effective areas

at the beginning of the mission should be higher than in 2010. However, many published studies indicated that the ground calibration in the SW channel was reasonable for the 2007 data, except for the shorter wavelengths, as shown in Del Zanna (2013a). Wang et al. (2011) performed a direct comparison between EIS SW and EUNIS quiet Sun (QS) observations in 2007, finding a small (20%) decrease compared

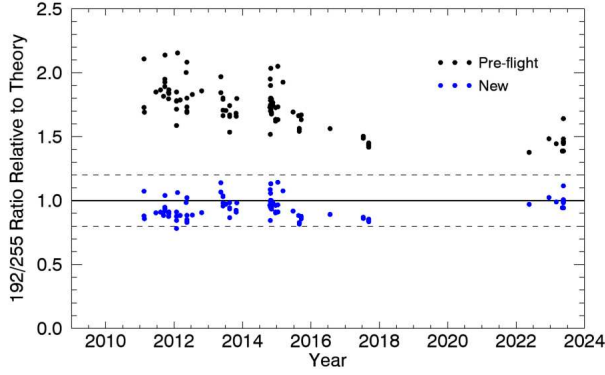


**Figure 8.** The Fe XXIV 192/255 Å ratio relative to theory as a function of time using the pre-flight calibration and the present time-dependant effective areas.

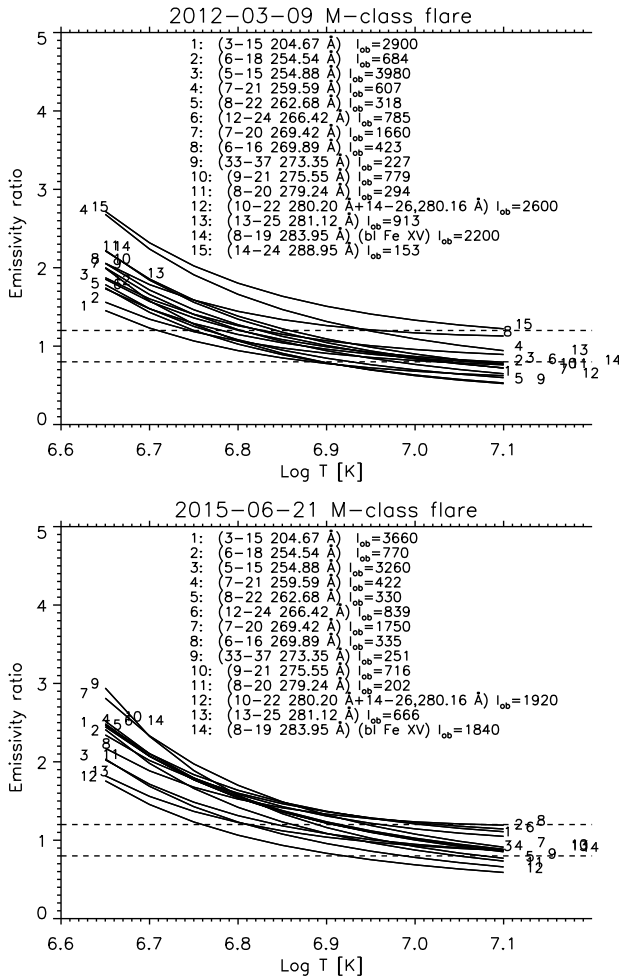


**Figure 9.** Emissivity ratio curves obtained with the present calibration for the main Fe XVII EUV transitions observed by Hinode EIS during two M-class flares, on 2012 March 9 and 2015 June 21.  $I_{\text{ob}}$  is the calibrated measured intensity in photons  $\text{cm}^{-2} \text{s}^{-1} \text{arcsec}^{-2}$ .

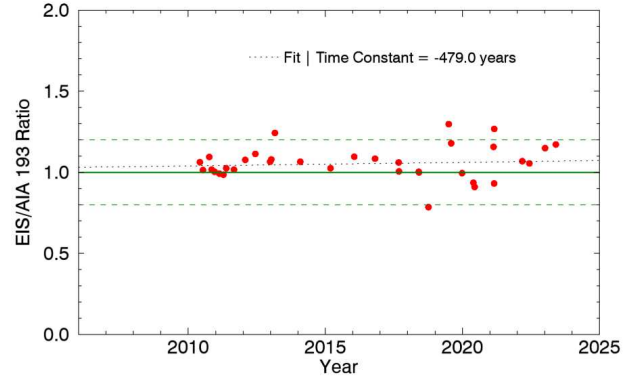
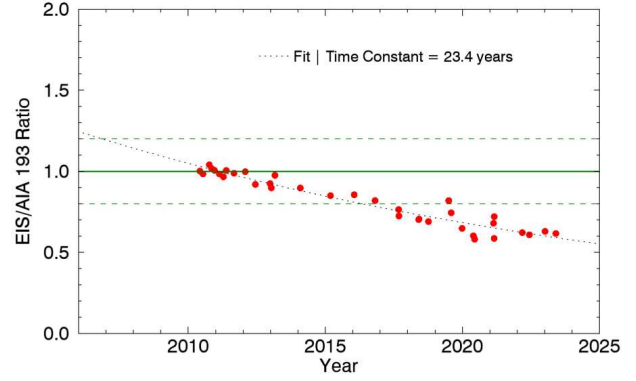


**Figure 10.** The ratio of EIS 193 to AIA 193 Å as a function of time using the pre-flight calibration (top panel) and the new, time-dependant effective areas (bottom panel). The EIS intensities have been convolved with the AIA 193 effective area to compute the expected AIA 193 count rates.

to the ground calibration, a variation within the EUNIS calibration uncertainties.

Another way to assess the calibration is to check that the quiet Sun calibrated radiances in low-temperature lines agree with literature values. There is always a scatter in the radiances of the quiet Sun, but on average they are relatively constant and largely independent of the solar cycle. In fact, they have been used for the in-flight calibration of the SOHO CDS instrument (cf Del Zanna & Andretta 2015; Andretta & Del Zanna 2014). As in Del Zanna (2013a), we have checked that the calibrated radiances are within 20–30% the literature values, for the few lines for which measurements were found. Furthermore, we have carried out an emission measure analysis using averaged quiet Sun CDS and EIS radiances, to check that we have consistency within 20%. Results will be discussed in a separate paper.

#### 4.8. Effective areas

Figure 11 shows the changes in the fit effective areas over time. The top two panels show the full 2D histograms for all wavelengths in each wave channel and the bottom two panels contain the values at select lines near the peaks and tails

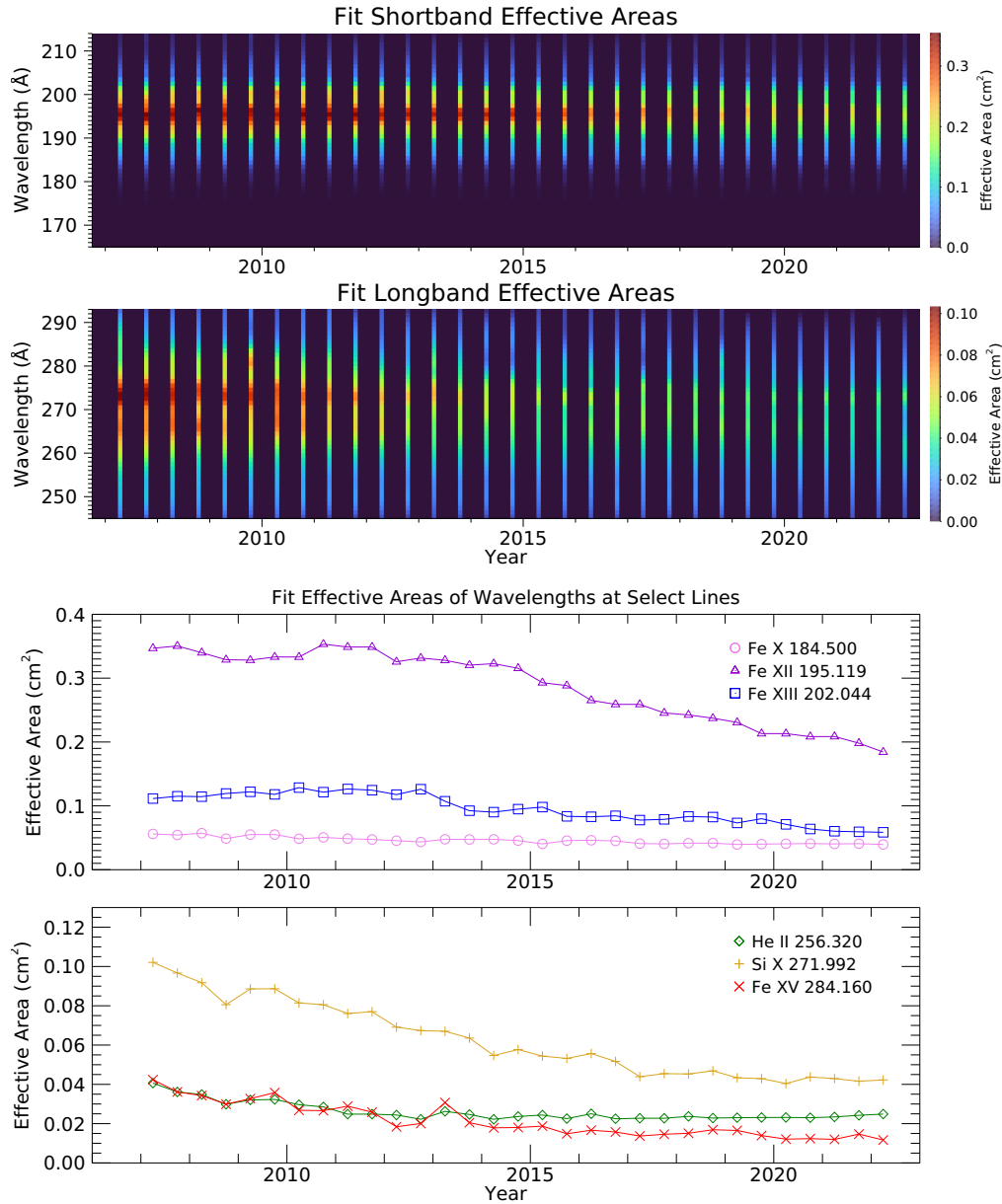


**Figure 11.** 2D histograms of the effective areas in the shortwave (top panel) and longwave (second panel) channels. Also shown are the effective areas at selected wavelengths near the peak and tails of the shortwave (third panel) and longwave (fourth panel) channels.

of each wave channel. The SW band (first and third panels) exhibit relatively little change until late 2012 and then a gradual decline in sensitivity after. In contrast, the sensitivity in the LW band (second and fourth panels) declines much faster at first, but then appears to plateau after 2017. Additionally, the LW band is more variable, which may indicate that the fit in that channel is more susceptible to outliers. This complex, channel-dependent decay in sensitivity is similar to the trends noted by Warren et al. (2014) for the years 2007 – 2013.

## 5. CONCLUSIONS

After trying several approaches we have presented what we believe is the best combination of methods, to provide a reasonable in-flight radiometric calibration for EIS. Overall, it provides calibrated intensities which should be accurate to within  $\pm 20\%$ . The overall degradation over time in the central parts of the two channels has been less than a factor of two over the 2006-2022 period, which is an excellent performance, one of the best of any EUV instrument in space, and the best of any EUV spectrometer (SOHO CDS degraded by a factor of about 2 in 13 years, see Del Zanna & Andretta 2015). Significant degradation is however present in various spectral regions.

As we have not found any evidence for systematic wavelength-dependent degradation, we do not have an explanation for the unusual evolution of the effective areas. Nearly all previous EUV/UV space instruments have shown significant degradation (see e.g. BenMoussa et al. 2013), which was usually thought to be associated with polymerization of chemical compounds (mostly including carbon) onto the surfaces of the front filters, caused by exposure to the strong solar flux. Such degradation is typically wavelength-dependent and the simple aluminium filters, used for the EUV (as for Hinode EIS), are particularly affected. Recently, it has been found that oxidation, caused by outgassing of water molecules, has also been causing major degradation for SDO instruments, see e.g. Tarrío et al. (2023). It seems unlikely that there is contamination on the EIS detector itself. Three EIS detector bakeouts were performed (2016 February 23–26, 2017 August 8–10, and 2018 January 17–21) and no sig-

nificant changes in response have been observed (see Figure 10).

We have biased the effective areas to keep a relatively smooth behaviour over time, associated with the degradation of the multilayers. Some wavelength regions are not well constrained, and a more accurate relative calibration could be obtained by analysing line ratios observed close in time to a specific observation.

Continuous monitoring of the degradation is recommended, by running EIS atlases in quiet Sun on-disk and off-limb regions, with exposure times of at least 60s, and off-limb active regions, with exposures of at least 30s.

#### Acknowledgments

GDZ acknowledges support from STFC (UK) via the consolidated grants to the atomic astrophysics group (AAG) at DAMTP, University of Cambridge (ST/P000665/1. and ST/T000481/1). HPW and MJW were supported by NASA's Hinode program.

#### REFERENCES

- Andretta, V., & Del Zanna, G. 2014, *A&A*, 563, A26, doi: [10.1051/0004-6361/201322841](https://doi.org/10.1051/0004-6361/201322841)
- BenMoussa, A., Gissot, S., Schühle, U., et al. 2013, *SoPh*, 288, 389, doi: [10.1007/s11207-013-0290-z](https://doi.org/10.1007/s11207-013-0290-z)
- Culhane, J. L., Harra, L. K., James, A. M., et al. 2007, *SoPh*, 60, doi: [10.1007/s01007-007-0293-1](https://doi.org/10.1007/s01007-007-0293-1)
- Del Zanna, G. 2008, *A&A*, 481, L69, doi: [10.1051/0004-6361:20079033](https://doi.org/10.1051/0004-6361:20079033)
- Del Zanna, G. 2013a, *A&A*, 555, A47, doi: [10.1051/0004-6361/201220810](https://doi.org/10.1051/0004-6361/201220810)
- . 2013b, *A&A*, 558, A73, doi: [10.1051/0004-6361/201321653](https://doi.org/10.1051/0004-6361/201321653)
- Del Zanna, G. 2019, *A&A*, 624, A36, doi: [10.1051/0004-6361/201834842](https://doi.org/10.1051/0004-6361/201834842)
- Del Zanna, G., & Andretta, V. 2015, *A&A*, 584, A29, doi: [10.1051/0004-6361/201526804](https://doi.org/10.1051/0004-6361/201526804)
- Del Zanna, G., Berrington, K. A., & Mason, H. E. 2004, *A&A*, 422, 731
- Del Zanna, G., Dere, K. P., Young, P. R., & Landi, E. 2020, *ApJS*, submitted
- Del Zanna, G., Dere, K. P., Young, P. R., Landi, E., & Mason, H. E. 2015, *A&A*, 582, A56, doi: [10.1051/0004-6361/201526827](https://doi.org/10.1051/0004-6361/201526827)
- Del Zanna, G., Gupta, G. R., & Mason, H. E. 2019, *A&A*, 631, A163, doi: [10.1051/0004-6361/201834625](https://doi.org/10.1051/0004-6361/201834625)
- Del Zanna, G., & Ishikawa, Y. 2009, *A&A*, 508, 1517, doi: [10.1051/0004-6361/200911729](https://doi.org/10.1051/0004-6361/200911729)
- Del Zanna, G., & Mason, H. E. 2005, *A&A*, 433, 731, doi: [10.1051/0004-6361:20041848](https://doi.org/10.1051/0004-6361:20041848)
- Del Zanna, G., & Mason, H. E. 2018, *Living Reviews in Solar Physics*, 15
- Del Zanna, G., O'Dwyer, B., & Mason, H. E. 2011, *A&A*, 535, A46, doi: [10.1051/0004-6361/201117470](https://doi.org/10.1051/0004-6361/201117470)
- Del Zanna, G., Polito, V., Dudík, J., et al. 2022, *ApJ*, 930, 61, doi: [10.3847/1538-4357/ac6174](https://doi.org/10.3847/1538-4357/ac6174)
- Lemen, J. R., Title, A. M., Akin, D. J., et al. 2012, *SoPh*, 275, 17, doi: [10.1007/s11207-011-9776-8](https://doi.org/10.1007/s11207-011-9776-8)
- Li, W., Yang, Y., Tu, B., et al. 2016, *ApJ*, 826, 219, doi: [10.3847/0004-637X/826/2/219](https://doi.org/10.3847/0004-637X/826/2/219)
- Lörinčík, J., Dudík, J., del Zanna, G., Dzifčáková, E., & Mason, H. E. 2020, *ApJ*, 893, 34, doi: [10.3847/1538-4357/ab8010](https://doi.org/10.3847/1538-4357/ab8010)
- Markwardt, C. B. 2009, in *Astronomical Society of the Pacific Conference Series*, Vol. 411, *Astronomical Data Analysis Software and Systems XVIII*, ed. D. A. Bohlender, D. Durand, & P. Dowler, 251, doi: [10.48550/arXiv.0902.2850](https://doi.org/10.48550/arXiv.0902.2850)
- Tarrío, C., Lucatorro, T. B., Berg, R. F., et al. 2023, *SoPh*, 298, 32, doi: [10.1007/s11207-023-02112-x](https://doi.org/10.1007/s11207-023-02112-x)
- Wang, T., Thomas, R. J., Brosius, J. W., et al. 2011, *ApJS*, 197, 32, doi: [10.1088/0067-0049/197/2/32](https://doi.org/10.1088/0067-0049/197/2/32)
- Warren, H. P., Brooks, D. H., & Winebarger, A. R. 2011, *ApJ*, 734, 90, doi: [10.1088/0004-637X/734/2/90](https://doi.org/10.1088/0004-637X/734/2/90)
- Warren, H. P., Ugarte-Urra, I., & Landi, E. 2014, *ApJS*, 213, 11, doi: [10.1088/0067-0049/213/1/11](https://doi.org/10.1088/0067-0049/213/1/11)
- Young, P. R., Watanabe, T., Hara, H., & Mariska, J. T. 2009, *A&A*, 495, 587, doi: [10.1051/0004-6361:200810143](https://doi.org/10.1051/0004-6361:200810143)

## APPENDIX

## A. EXTRA INFORMATION ON QS AND AR DATA

The QS on-disk observations, with exposure times of 60 or 120 s and the 2'' slit have been averaged spatially before fitting the lines to obtain DN/s. Most of the observations were using the ATLAS\_60 or ATLAS\_120. Table 2 gives the list of the files analysed.

Fig. 12 gives as an example three of those spectra, taken near the beginning of the mission in 2008, in 2012, and 2017. Some of the hotter lines have a strong variability with the solar cycle and location, but those formed at 1 MK and below are not expected to show strong variability (see, e.g. the discussion in [Del Zanna & Andretta 2015](#), related to the SOHO/CDS calibration). The figure shows the clear decrease in the signal with time, and the fact that the shorter and longer wavelengths of the LW channel degraded significantly already by 2017.

**Table 2.** List of the quiet Sun EIS observations analysed.

20140811_032251	20150322_100148	20150523_191534	20150824_090730	20151117_030548
20160117_090447	20160322_032503	20160411_221723	20160828_104853	20161009_163155
20161119_111934	20161217_111122	20170604_110854	20170816_113050	20170914_155935
20171105_150928	20180114_130641	20180612_000414	20180808_185533	20180830_041726
20181026_133649	20181225_204342	20190227_041730	20190421_160905	20190629_034213
20190906_002026	20191019_021112	20191212_224436	20200229_150606	20200531_145440
20200701_132213	20200925_025943	20201102_071219	20210302_221641	20210312_044443
20210403_182040	20210716_024902	20210810_164920	20211013_031242	20211130_140230
20211224_021532	20220307_160313	20220601_042513		

For the active region datasets, most of the data were from the ATLAS\_30 or ATLAS\_60. Table 3 lists the EIS files analysed. Whenever available, off-limb observations were used.

**Table 3.** List of the active region EIS observations analysed.

20061225_225013	20070118_120435	20070220_054028	20070511_105544	20070714_000949
20071114_000707	20080107_101448	20080204_104700	20080620_230339	20081217_110519
20090322_060630	20090521_180529	20090725_055049	20091025_214625	20100123_171532
20100517_135741	20100922_112633	20101109_100733	20110121_123757	20110522_103354
20110726_175935	20111022_100543	20111217_125856	20120416_124033	20120704_223657
20120830_234044	20130127_081649	20130327_021709	20130601_115857	20130915_151340
20131104_075110	20140114_122452	20140508_182049	20140718_132530	20141013_111316
20141223_102142	20150322_215524	20150615_195749	20151022_014109	20151230_182726
20160317_203054	20160530_213525	20160804_081348	20161001_182941	20161210_202027
20170208_111733	20170503_115341	20170802_130640	20171008_014841	20171202_000340
20180117_085140	20180612_032114	20180810_083243	20181006_141212	20181216_101341
20190130_234741	20190326_130041	20190615_182748	20190628_093832	20190903_111822
20191011_235843	20191224_213813	20200202_133341	20200503_112000	20200615_004741
20200806_001010	20201006_111549	20201115_214810	20201202_112940	20210228_155913
20210420_200014	20210529_151812	20210802_224611	20210903_084840	20211104_030841
20211226_120039	20220306_232633	20220428_234108	20220807_142340	

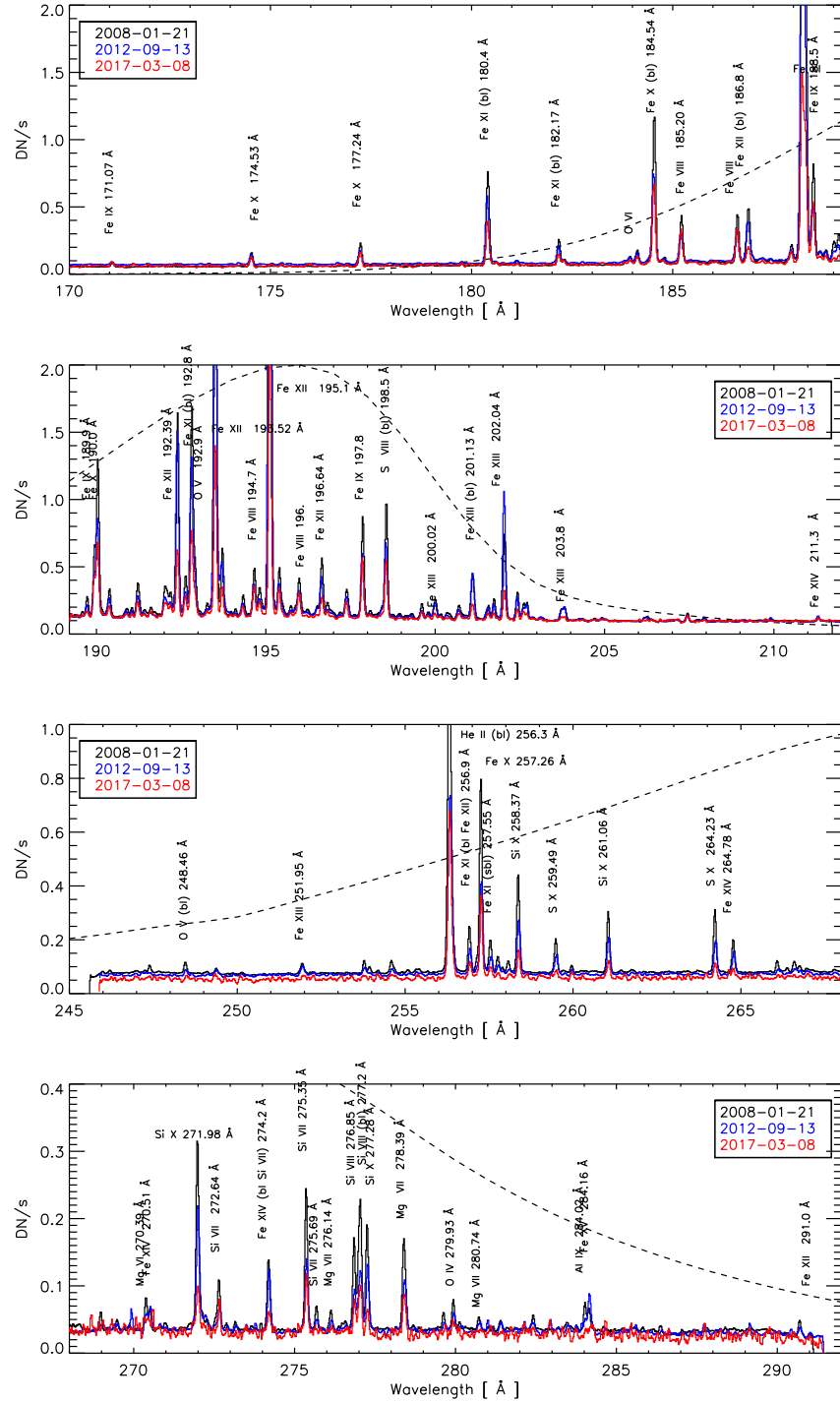


**Figure 12.** Hinode EIS spectra (DN/s/1" slit) for the quiet Sun on-disk, for three sample dates. The dashed line is the scaled ground-calibration effective area.

## B. SELECTED LINE RATIOS

Table 4 lists the line ratios selected for the EIS relative calibration. The best ones are branching ratios, as they do not depend on electron density and have a small theoretical uncertainty, of the order of 10%. The other ratios have a larger typical uncertainty, around 20%. We then used different ratios for the QS and AR observations. Some ratios have some small density sensitivity,

which we list in the Table. Most ratios are useful to constrain the relative calibration within the SW and LW, but some are also available to check the SW/LW relative ratio.

**Table 4.** Line ratios used for the EIS calibration. The second and third columns show the theoretical ratios (photon units) for suitable densities for the QS and AR. The last column indicates the channel. BR indicates a branching ratio.

Line ratio (Å)	Predicted (QS) (log Ne=8.2–8.8)	Predicted (AR) 8.5–9.5	Notes	Det.
Fe IX 189.94 / 197.85	1.0–1.2	1.1–1.5 **		SW
Fe IX 188.49 / 197.85	2.0–2.1	2.0–2.5 **		SW
Fe X 174.5 / 184.5	4.5–4.4	4.45–4.0		SW
Fe X 177.2 / 184.5	2.6–2.5	2.58–2.35		SW
Fe X 190.0 (bl) / 184.5	0.338			BR SW
Fe X 207.45 / 184.5	0.14–0.16	0.15–0.21 **		SW
Fe X 257.3 (sbl) / 184.5	1.5–1.2	1.35–0.8 **		LW/SW
Fe XI 178.1 / 182.17	0.274		weak	BR SW
Fe XI 188.2 / 192.8 (bl)	4.8			BR SW
Fe XI 202.7 / 188.3	0.1			BR SW
Fe XI 180.4 / 188.2	2.0–1.98	1.99–1.88		SW
Fe XI 257.5 (sbl) / 188.2	0.17–0.19	0.175–0.24 **		LW/SW
Fe XII 192.4 / 195.1 (sbl)	0.315			SW
Fe XII 193.5 / 195.1 (sbl)	0.67			SW
Fe XII 186.9 (sbl) / 196.6 (bl)	3.45–3.6	3.5–4.1 **		SW
Fe XIII 209.9 (bl) / 202.0	0.15			BR SW
Fe XIII 204.9 (bl) / 201.1 (bl)	0.31			BR SW
Fe XIII 201.1 (bl) / 197.4	5.0			BR SW
Fe XIII 204.9 (bl) / 197.4	1.55			BR SW
Fe XIII 209.6 / 200.	0.74–0.69	0.69–0.71		SW
Fe XIII 246.2 (bl?) / 251.9	0.51			BR LW
Fe XIII 261.7 / 251.9	0.135–0.12	0.125–0.105		LW
Fe XIII 261.7 / 201.1 (bl)	0.185–0.17	0.17–0.18		LW/SW
Fe XIII 251.9 / 201.1 (bl)	1.35–1.45	1.4–1.65 **		LW/SW
Fe XIII 251.9 / 204.9	4.6–4.9	4.7–5.5 **		LW/SW
Fe XIV 252.2 / 264.8	0.23			BR LW
Fe XIV 257.4 / 270.5	0.68			BR LW
Fe XIV 289.1 / 274.2	0.065		weak	BR LW
Fe XIV 274.2 / 211.3	0.71	0.71–0.69		LW/SW
Fe XIV 270.5 / (264.7+274.2)	0.265	0.265–0.255		LW
Fe XVI 251 / 263	0.57	0.57		LW
Fe XVI 265 / 263	0.098	0.098		LW
Fe XVII 254.9 / 204.7	1/0.93			BR LW/SW
Fe XXIV 255.1 / 192	1/1.85			LW/SW
Si X 253.8 / 258.4	0.194			BR LW
Si X 277.3 / 272.	0.84			BR LW
Si X 277.3 / 261.1	0.68	0.68–0.70		LW
S X 257.1 (bl) / 264.2	0.348	0.348		LW
S X 259.5 / 264.2	0.68	0.68		LW
S XI 285.6 (sbl) / 281.4	0.496			BR LW

### C. ABSOLUTE CALIBRATION AFTER 2010: EIS VS. AIA

As a first step, the EIS data were processed with `eis_prep` and the pre-flight calibration. The AIA 193 Å data were cutouts downloaded from the JSOC with an expanded FOV relative to EIS and a cadence of 36 s. These data are processed with `aia_prep`.

For each EIS exposure, the background was estimated, and the spectrum convolved with the AIA effective area (EA) calculated using the `evenorm` and `timedepend_date` keywords, to compute the expected AIA counts. The nearest 3 AIA images were found and averaged. The averaged was then smoothed over 5 pixels ( $3''$ ) and rebinned to the EIS pixel size of  $1''$ . The predicted and observed AIA images were then cross-correlated to find the optimal EIS pointing, i.e. finding (`aia_x`, `aia_y`), the position of the bottom of the eis slit derived from AIA. Since the cross correlation is done exposure by exposure, it can be noisy, particularly if there is little structure along the slit. We expect that the `aia_y` values should all be very similar and the `aia_x` values to increase linearly with time due to solar rotation. A second pass is then computed, and a mean `aia_y` and a linear fit to `aia_x` obtained.

#### D. NORMALIZED EMISSIVITY CURVES

Density-sensitive line ratios are often used in the literature to measure the electron density. Such measurements rely on accurate atomic data and relative radiometric calibration. As the EIS effective area has a strong wavelength variation, any small change in the relative effective area can affect the density measurements significantly. We have checked for a sample of dates that the electron densities obtained from the main line ratios and ions are reasonable, using the emissivity ratio method, described in the main part of the paper. Fig. 13 shows one example for the main coronal lines. We expected the ratio curves to intersect, providing a density measurements, although in principle some departures can occur, as each transition is likely formed in a slightly different spatial region. The curves of the strong Fe XII lines at 192.4, 193.5, 195.1 Å often show discrepancies, related to opacity effects. The weaker transition at 192.4 Å is less affected and should be used for the density measurements. We do not expect that densities measured by different ions should be exactly the same, but those of the Fe XII, Fe XIII and Si X should be consistent, as these ions are formed within similar temperatures. The emissivity ratios in the off-limb QS regions generally show better agreement than those in active regions, as one would expect.

#### E. ON-DISK AR LOOP DEM ANALYSIS

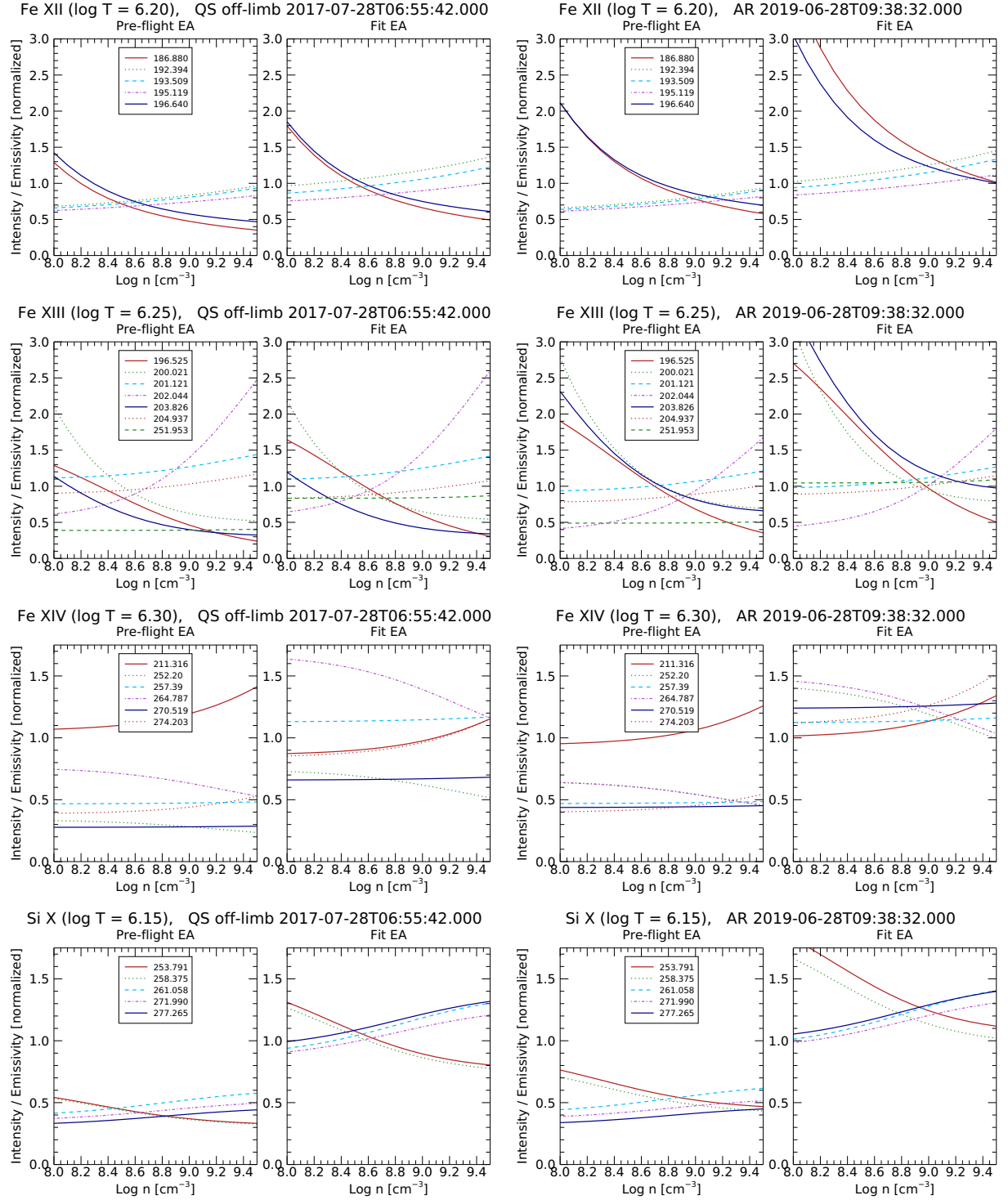
As in the QS off-limb case, we have used a constant density assumption to obtain the  $G(T)$  of the lines. The temperature distributions typically have multiple peaks, one around  $\log T[\text{K}]=5.6$  produced by the loop legs, and other ones due to the background/foreground coronal plasma present in the AR core.

Table 5 lists the main lines. The most useful lines are from Fe VIII, as they cover both SW and LW. The stronger lines are well represented within  $\pm 10\%$ . The Fe IX lines are also useful to check the SW sensitivity, especially at the location of the resonance line at 171.0 Å, as this line is always very weak in any QS observation. The three LW lines from Si VII are in good agreement with those from Fe VIII, while other lines show larger departures. The O V 192.9 vs 248.5 Å ratio is not very reliable as lines are weak and are both temperature and density sensitive.

#### F. OFF-LIMB DEM ANALYSIS

Tables 6,7,8, 9,10,11, 12 show the summary results of the DEM analysis for the main (strongest) coronal lines, in off-limb observations. Note that in the last observation hotter active region plasma was present.

The calibrated intensities were obtained by manual adjustment of the ground calibration effective area, using splines with nodes at 165, 171, 174.5, 177.2, 178.1, 180.4, 182.2, 184.5, 185.2, 186.9, 188.3, 190, 192.4, 192.8, 193.5, 194.7, 195.1, 196.6, 197.4, 200, 201.1, 202., 202.7, 204.9, 208, 209.9, 211.3 Å for the SW channel, and 245, 252, 255, 257, 259, 263, 265, 268, 270, 272, 274, 277, 281, 286, 292 Å for the LW channel. These wavelengths are close to main coronal lines. The absolute scale of the calibration was adjusted with a preliminary cross-calibration with AIA. These effective areas were used as initial constraint on the final effective areas, obtained by automatic fitting the line ratios.



**Figure 13.** Normalized emissivity curves for Fe XII, Fe XIII, Fe XIV, and Si X. The left two columns show the curves computed using the pre-flight and fit effective areas for a QS off-limb subregion observed on 2017-07-28. The right two columns show the results for a subregion containing an AR observed on 2019-06-28.

**Table 5.** Same as Table 1, but for an AR loop observation on 26 Oct 2010

$\lambda_{\text{obs}}$	DN	$I_{\text{obs}}$	$\log T_{\text{max}}$	$\log T_{\text{eff}}$	$R$	Ion	$\lambda_{\text{exp}}$	$r$
192.91	2690	170.9	5.42	5.56	1.38	O v	192.904	0.84
248.49	260	319.8	5.42	5.58	0.87	O v	248.461	0.91
276.58	1210	296.1	5.50	5.59	0.74	Mg v	276.579	0.98
246.00	524	799.5	5.64	5.67	0.46	Si vi	246.003	0.98
270.39	3630	887.6	5.65	5.68	0.36	Mg vi	270.400	0.12
						Mg vi	270.391	0.87
268.99	1720	464.9	5.66	5.68	0.34	Mg vi	268.991	0.98
255.11	252	130.6	5.66	5.73	0.96	Fe viii	255.110	0.99
255.35	391	197.3	5.67	5.73	1.03	Fe viii	255.350	0.96
253.96	509	306.6	5.67	5.74	1.06	Fe viii	253.956	0.99
195.97	5720	298.8	5.31	5.75	1.12	Fe viii	195.972	0.92
207.12	286	183.7	5.70	5.76	0.93	Fe viii	207.124	0.73
						Fe viii	207.124	0.25
197.36	3050	172.6	5.71	5.76	0.84	Fe viii	197.362	0.97
194.66	8270	442.0	5.72	5.76	1.17	Fe viii	194.661	0.99
186.60	8150	1573.1	5.73	5.80	1.03	Fe viii	186.598	0.96
185.22	7630	2116.2	5.73	5.80	1.09	Fe viii	185.213	0.97
280.74	849	304.8	5.79	5.82	0.64	Mg vii	280.742	0.98
276.14	613	146.1	5.79	5.83	0.66	Mg vii	276.154	0.98
275.37	2660	612.9	5.79	5.83	1.03	Si vii	275.361	0.98
275.69	458	106.8	5.80	5.83	1.05	Si vii	275.676	0.98
272.66	940	183.8	5.80	5.83	1.07	Si vii	272.648	0.98
278.39	3270	907.6	5.79	5.83	0.53	Mg vii	278.404	0.97
277.00	2460	615.3	5.84	5.87	0.80	Mg vii	277.003	0.57
						Si viii	277.058	0.39
276.84	953	236.0	5.87	5.88	1.26	Si viii	276.850	0.47
						Si vii	276.851	0.48
171.07	122	8739.7	5.93	5.91	0.92	Fe ix	171.073	0.99
189.94	2450	250.6	5.94	5.92	0.94	Fe ix	189.935	0.97
191.21	1770	150.2	5.94	5.92	0.69	Fe ix	191.206	0.98
188.49	3240	432.2	5.94	5.93	1.00	Fe ix	188.493	0.91
197.85	2760	162.7	5.96	5.94	1.01	Fe ix	197.854	0.95
190.04	2370	239.2	6.05	6.04	1.07	Fe x	190.037	0.68
						Fe ix	190.059	0.17

**Table 6.** Same as Table 1, but for a QS off-limb observation on 16 Oct 2010

$\lambda_{\text{obs}}$	DN	$I_{\text{obs}}$	$\log T_{\text{max}}$	$\log T_{\text{eff}}$	$R$	Ion	$\lambda_{\text{exp}}$	$r$
194.66	238	6.4	5.72	6.02	1.27	Fe VIII	194.661	0.94
185.22	218	30.3	5.73	6.03	1.30	Fe VIII	185.213	0.93
186.60	222	23.0	5.73	6.04	1.30	Fe VIII	186.598	0.86
189.94	382	19.6	5.94	6.10	1.24	Fe IX	189.935	0.97
188.49	728	52.4	5.95	6.10	0.97	Fe IX	188.493	0.89
197.85	886	26.0	5.96	6.11	1.01	Fe IX	197.854	0.93
257.26	1030	214.5	6.04	6.13	0.98	Fe X	257.259	0.22
						Fe X	257.263	0.76
177.24	204	646.7	6.05	6.14	1.03	Fe X	177.240	0.97
174.53	108	1101.1	6.05	6.14	1.07	Fe X	174.531	0.98
184.54	1700	281.6	6.05	6.14	0.89	Fe X	184.537	0.95
190.04	2170	109.3	6.06	6.15	1.05	Fe XII	190.040	0.19
						Fe X	190.037	0.68
257.55	322	65.2	6.12	6.16	1.25	Fe XI	257.554	0.69
						Fe XI	257.547	0.26
189.02	298	18.9	6.13	6.16	0.73	Fe XI	188.997	0.95
256.92	492	104.7	6.12	6.16	0.97	Fe XI	256.919	0.91
182.17	507	193.2	6.13	6.16	0.98	Fe XI	182.167	0.97
192.81	4550	160.2	6.13	6.16	0.89	Fe XI	192.813	0.96
188.30	5980	448.3	6.13	6.16	0.92	Fe XI	188.299	0.97
181.13	95	57.3	6.13	6.16	1.13	Fe XI	181.130	0.97
188.22	9530	726.2	6.13	6.16	0.92	Fe XI	188.216	0.97
180.40	1630	1340.4	6.13	6.17	1.05	Fe XI	180.401	0.97
180.60	69	52.7	6.13	6.17	0.88	Fe XI	180.594	0.96
202.71	423	47.3	6.13	6.17	1.23	Fe XI	202.705	0.92
253.79	167	51.5	6.15	6.17	0.93	Si X	253.790	0.97
258.37	1300	248.6	6.15	6.17	0.98	Si X	258.374	0.97
261.06	845	135.0	6.15	6.17	0.99	Si X	261.056	0.98
271.99	1200	116.5	6.15	6.17	0.95	Si X	271.992	0.97
277.27	687	87.2	6.15	6.17	0.98	Si X	277.264	0.98
256.40	1030	229.8	6.16	6.18	1.18	Si X	256.377	0.59
						Fe XIII	256.400	0.12
						Fe XII	256.410	0.18
249.39	114	65.0	6.19	6.19	0.86	Fe XII	249.388	0.70
						Fe XII	249.384	0.23
196.64	1900	51.4	6.19	6.19	1.16	Fe XII	196.640	0.93
186.88	2310	225.8	6.19	6.19	0.98	Fe XII	186.854	0.16
						Fe XII	186.887	0.77
193.51	22900	765.5	6.19	6.19	1.02	Fe XII	193.509	0.95
195.12	36200	852.8	6.19	6.19	1.32	Fe XII	195.119	0.97
192.39	9820	343.6	6.19	6.19	1.05	Fe XII	192.394	0.96
196.52	674	18.1	6.24	6.21	1.21	Fe XIII	196.525	0.92
200.02	1420	59.2	6.25	6.21	0.93	Fe XIII	200.021	0.95
261.73	136	20.9	6.25	6.22	1.17	Fe XIII	261.743	0.97
203.83	1430	229.6	6.25	6.22	1.06	Fe XIII	203.795	0.28
						Fe XIII	203.826	0.63
246.21	142	106.4	6.25	6.22	1.02	Fe XIII	246.209	0.95
251.95	483	193.3	6.25	6.22	1.03	Fe XIII	251.952	0.97
204.94	248	53.5	6.25	6.22	0.98	Fe XIII	204.942	0.96
209.92	271	144.5	6.25	6.22	0.94	Fe XIII	209.916	0.96
202.04	9310	819.2	6.25	6.22	0.95	Fe XIII	202.044	0.97
264.79	1300	181.7	6.29	6.23	0.97	Fe XIV	264.789	0.81
						Fe XI	264.772	0.15
274.20	1890	223.8	6.29	6.24	0.98	Fe XIV	274.204	0.96
252.20	81	31.6	6.29	6.24	1.16	Fe XIV	252.200	0.95
289.15	26	19.9	6.29	6.24	0.92	Fe XIV	289.151	0.96
270.52	814	96.7	6.29	6.24	1.00	Fe XIV	270.521	0.96
257.40	221	45.3	6.29	6.24	1.53	Fe XIV	257.394	0.96
211.32	632	392.7	6.29	6.24	1.00	Fe XIV	211.317	0.96
284.16	1560	508.3	6.34	6.27	1.01	Fe XV	284.163	0.96

**Table 7.** Same as Table 1, but for a QS off-limb observation on 7 Oct 2013

$\lambda_{\text{obs}}$	DN	$I_{\text{obs}}$	$\log T_{\text{max}}$	$\log T_{\text{eff}}$	$R$	Ion	$\lambda_{\text{exp}}$	$r$
194.66	513	11.7	5.72	6.01	0.88	Fe VIII	194.661	0.94
186.60	514	38.9	5.73	6.04	1.00	Fe VIII	186.598	0.82
185.22	365	45.3	5.73	6.05	1.17	Fe VIII	185.213	0.86
189.94	566	26.7	5.94	6.10	1.12	Fe IX	189.935	0.95
188.49	954	60.3	5.95	6.11	1.03	Fe IX	188.493	0.83
197.85	981	28.0	5.96	6.11	1.10	Fe IX	197.854	0.91
257.26	1130	268.7	6.04	6.15	0.90	Fe X	257.259	0.24
						Fe X	257.263	0.74
177.24	354	824.7	6.05	6.15	0.97	Fe X	177.240	0.97
174.53	188	1328.5	6.05	6.15	1.07	Fe X	174.531	0.97
184.54	2230	330.4	6.05	6.16	0.93	Fe X	184.537	0.94
190.04	3100	142.8	6.06	6.17	1.06	Fe XII	190.040	0.23
						Fe X	190.037	0.63
184.79	207	28.8	6.12	6.18	1.05	Fe XI	184.793	0.94
257.55	479	110.9	6.12	6.18	1.02	Fe XI	257.554	0.68
						Fe XI	257.547	0.26
256.92	725	175.9	6.12	6.18	0.78	Fe XI	256.919	0.89
182.17	954	345.8	6.13	6.18	0.81	Fe XI	182.167	0.96
192.81	7840	220.4	5.42	6.18	0.90	Fe XI	192.813	0.96
181.13	204	106.4	6.13	6.18	0.91	Fe XI	181.130	0.97
188.30	8990	581.8	6.13	6.18	0.98	Fe XI	188.299	0.97
188.22	15900	1030.8	6.13	6.18	0.91	Fe XI	188.216	0.97
180.40	2880	1927.1	6.13	6.18	1.01	Fe XI	180.401	0.97
202.71	852	75.9	6.13	6.19	1.09	Fe XI	202.705	0.90
258.37	1990	435.5	6.15	6.19	0.88	Si X	258.374	0.97
253.79	278	88.5	6.15	6.19	0.85	Si X	253.790	0.97
271.99	1580	192.4	6.15	6.19	0.83	Si X	271.992	0.97
261.06	1260	229.3	6.15	6.19	0.84	Si X	261.056	0.98
277.27	836	133.8	6.15	6.19	0.91	Si X	277.264	0.98
256.40	1550	393.3	6.16	6.20	1.04	Si X	256.377	0.56
						Fe XIII	256.400	0.15
						Fe XII	256.410	0.20
249.39	184	91.0	6.19	6.20	1.00	Fe XII	249.388	0.71
						Fe XII	249.384	0.23
196.64	4250	107.1	6.19	6.20	1.04	Fe XII	196.640	0.94
186.88	5200	367.1	6.19	6.20	1.13	Fe XII	186.854	0.17
						Fe XII	186.887	0.76
193.51	40100	885.9	6.19	6.20	1.40	Fe XII	193.509	0.95
192.39	18200	550.9	6.19	6.20	1.05	Fe XII	192.394	0.96
195.12	63200	1284.7	6.19	6.20	1.40	Fe XII	195.119	0.97
196.52	1760	43.6	6.24	6.22	1.04	Fe XIII	196.525	0.93
200.02	3390	140.2	6.25	6.22	0.85	Fe XIII	200.021	0.95
261.73	241	42.2	6.25	6.22	1.02	Fe XIII	261.743	0.96
203.83	3600	440.5	6.25	6.22	1.21	Fe XIII	203.795	0.28
						Fe XIII	203.826	0.64
251.95	945	354.6	6.25	6.22	1.02	Fe XIII	251.952	0.97
204.94	706	121.4	6.25	6.22	0.77	Fe XIII	204.942	0.96
209.92	691	272.0	6.25	6.22	0.81	Fe XIII	209.916	0.96
202.04	18000	1466.4	6.25	6.22	0.86	Fe XIII	202.044	0.96
264.79	2210	353.0	6.29	6.23	0.92	Fe XIV	264.789	0.85
						Fe XI	264.772	0.11
274.20	3270	427.2	6.29	6.24	0.95	Fe XIV	274.204	0.96
252.20	186	68.2	6.29	6.24	1.03	Fe XIV	252.200	0.95
270.52	1460	204.2	6.29	6.24	0.89	Fe XIV	270.521	0.96
211.32	1670	986.8	6.29	6.24	0.74	Fe XIV	211.317	0.96
284.16	3350	1200.6	6.34	6.27	0.80	Fe XV	284.163	0.96
262.98	143	23.4	6.43	6.31	0.92	Fe XVI	262.976	0.63
						Fe XIII	262.984	0.32

**Table 8.** Same as Table 1, but for a QS off-limb observation on 7 Aug 2014

$\lambda_{\text{obs}}$	DN	$I_{\text{obs}}$	$\log T_{\text{max}}$	$\log T_{\text{eff}}$	$R$	Ion	$\lambda_{\text{exp}}$	$r$
194.66	272	13.1	5.72	6.05	1.09	Fe VIII	194.661	0.96
185.22	265	70.9	5.73	6.06	1.01	Fe VIII	185.213	0.93
186.60	315	60.7	5.73	6.06	0.91	Fe VIII	186.598	0.84
189.94	578	60.3	5.94	6.08	0.84	Fe IX	189.935	0.96
188.49	678	91.4	5.95	6.08	1.11	Fe IX	188.493	0.87
197.85	1060	64.9	5.96	6.08	0.78	Fe IX	197.854	0.95
257.26	928	470.9	6.04	6.09	0.72	Fe X	257.259	0.24
						Fe X	257.263	0.74
177.24	229	1152.0	6.05	6.10	0.92	Fe X	177.240	0.98
174.53	117	1788.6	6.05	6.10	1.04	Fe X	174.531	0.98
184.54	1470	498.8	6.05	6.10	0.79	Fe X	184.537	0.97
190.04	1870	191.9	6.06	6.10	0.81	Fe X	190.037	0.80
256.92	303	157.6	6.12	6.11	0.72	Fe XI	256.919	0.93
181.13	69	77.8	6.13	6.11	0.99	Fe XI	181.130	0.96
182.17	317	247.8	6.13	6.11	0.90	Fe XI	182.167	0.97
192.81	2670	159.7	5.42	6.11	0.98	Fe XI	192.813	0.96
188.22	5080	718.5	6.13	6.11	1.03	Fe XI	188.216	0.98
188.30	3560	495.2	6.13	6.11	0.92	Fe XI	188.299	0.98
180.40	1020	1484.1	6.13	6.11	1.04	Fe XI	180.401	0.98
202.71	275	62.2	6.13	6.11	1.01	Fe XI	202.705	0.95
258.37	596	279.7	6.15	6.12	0.91	Si X	258.374	0.97
253.79	75	50.0	6.15	6.12	1.01	Si X	253.790	0.97
256.40	511	275.1	6.16	6.12	0.89	Si X	256.377	0.62
						Fe XII	256.410	0.15
						Fe X	256.398	0.14
271.99	451	117.8	6.15	6.12	0.90	Si X	271.992	0.98
261.06	361	141.3	6.15	6.12	0.90	Si X	261.056	0.98
277.27	240	82.2	6.15	6.12	0.99	Si X	277.264	0.98
249.39	47	49.2	6.19	6.12	0.88	Fe XII	249.388	0.68
						Fe XII	249.384	0.21
196.64	836	45.2	6.19	6.13	1.08	Fe XII	196.640	0.93
186.88	872	158.9	6.19	6.13	1.12	Fe XII	186.854	0.17
						Fe XII	186.887	0.78
193.51	7550	387.7	6.19	6.13	1.34	Fe XII	193.509	0.94
192.39	3240	209.5	6.19	6.13	1.13	Fe XII	192.394	0.96
195.12	12100	528.0	6.19	6.13	1.40	Fe XII	195.119	0.97
264.79	187	63.9	6.29	6.14	0.90	Fe XIV	264.789	0.44
						Fe XI	264.772	0.53
200.02	394	34.6	6.25	6.14	0.73	Fe XIII	200.021	0.91
203.83	255	78.7	6.25	6.14	1.37	Fe XIII	203.795	0.28
						Fe XIII	203.826	0.64
251.95	90	70.6	6.25	6.14	1.03	Fe XIII	251.952	0.96
209.92	42	35.3	6.25	6.14	1.22	Fe XIII	209.916	0.94
204.94	48	18.5	6.25	6.14	1.00	Fe XIII	204.942	0.95
202.04	1620	286.4	6.25	6.15	0.85	Fe XIII	202.044	0.96
274.20	135	42.3	6.29	6.15	0.96	Fe XIV	274.204	0.87
211.32	60	77.2	6.29	6.16	0.86	Fe XIV	211.317	0.94
270.52	65	19.6	6.29	6.16	0.84	Fe XIV	270.521	0.96
284.16	45	34.9	6.34	6.19	1.14	Fe XV	284.163	0.96

**Table 9.** Same as Table 1, but for a QS off-limb observation on 6 Aug 2016

$\lambda_{\text{obs}}$	DN	$I_{\text{obs}}$	$\log T_{\text{max}}$	$\log T_{\text{eff}}$	$R$	Ion	$\lambda_{\text{exp}}$	$r$
194.66	116	6.4	5.72	6.04	0.90	Fe VIII	194.661	0.91
185.22	110	25.5	5.73	6.06	1.17	Fe VIII	185.213	0.83
186.60	147	24.4	5.73	6.07	0.91	Fe VIII	186.598	0.77
189.94	185	19.0	5.94	6.13	1.03	Fe IX	189.935	0.94
188.49	401	47.3	5.95	6.14	0.88	Fe IX	188.493	0.80
197.85	369	19.1	5.96	6.14	1.09	Fe IX	197.854	0.89
257.26	510	224.5	6.04	6.17	0.82	Fe X	257.259	0.23
						Fe X	257.263	0.74
174.53	92	1225.3	6.05	6.17	0.91	Fe X	174.531	0.97
177.24	166	718.4	6.05	6.17	0.87	Fe X	177.240	0.97
184.54	956	304.6	6.05	6.17	0.79	Fe X	184.537	0.93
190.04	1240	125.0	6.06	6.18	0.99	Fe XII	190.040	0.25
						Fe X	190.037	0.60
184.79	96	27.2	6.12	6.19	0.95	Fe XI	184.793	0.95
257.55	228	98.7	6.12	6.19	0.98	Fe XI	257.554	0.68
						Fe XI	257.547	0.26
189.02	199	22.3	6.13	6.19	0.94	Fe XI	188.997	0.95
256.92	324	146.4	6.12	6.19	0.80	Fe XI	256.919	0.89
182.17	383	258.9	6.13	6.19	0.93	Fe XI	182.167	0.96
192.81	3000	185.7	5.42	6.19	0.93	Fe XI	192.813	0.96
181.13	79	77.2	6.13	6.19	1.08	Fe XI	181.130	0.97
188.30	4060	489.6	6.13	6.19	1.01	Fe XI	188.299	0.97
188.22	6520	796.2	6.13	6.19	1.02	Fe XI	188.216	0.97
180.40	1320	1650.5	6.13	6.19	1.03	Fe XI	180.401	0.97
202.71	271	54.2	6.13	6.19	1.33	Fe XI	202.705	0.90
258.37	906	370.1	6.15	6.20	0.91	Si X	258.374	0.97
253.79	116	66.7	6.15	6.20	0.99	Si X	253.790	0.97
271.99	646	158.1	6.15	6.20	0.89	Si X	271.992	0.97
261.06	566	192.1	6.15	6.20	0.88	Si X	261.056	0.98
277.27	292	109.8	6.15	6.20	0.98	Si X	277.264	0.98
249.39	109	97.8	6.19	6.20	0.84	Fe XII	249.388	0.72
						Fe XII	249.384	0.23
196.64	1680	87.3	6.19	6.21	1.15	Fe XII	196.640	0.94
186.88	2280	360.3	6.19	6.21	1.05	Fe XII	186.854	0.17
						Fe XII	186.887	0.76
193.51	17800	951.5	6.19	6.21	1.18	Fe XII	193.509	0.95
195.12	27900	1319.5	6.19	6.21	1.24	Fe XII	195.119	0.97
192.39	7770	486.5	6.19	6.21	1.08	Fe XII	192.394	0.96
196.52	753	39.0	6.24	6.22	1.07	Fe XIII	196.525	0.93
200.02	1440	110.2	6.25	6.22	0.99	Fe XIII	200.021	0.95
261.73	108	35.1	6.25	6.22	1.12	Fe XIII	261.743	0.97
203.83	1580	444.0	6.25	6.22	1.10	Fe XIII	203.795	0.28
						Fe XIII	203.826	0.64
251.95	513	348.0	6.25	6.22	0.96	Fe XIII	251.952	0.97
204.94	266	94.3	6.25	6.22	0.91	Fe XIII	204.942	0.96
209.92	247	193.3	6.25	6.22	1.04	Fe XIII	209.916	0.96
202.04	7390	1136.1	6.25	6.22	1.02	Fe XIII	202.044	0.96
264.79	1070	318.3	6.29	6.23	0.91	Fe XIV	264.789	0.85
						Fe XI	264.772	0.11
274.20	1370	373.0	6.29	6.23	0.98	Fe XIV	274.204	0.96
252.20	97	64.5	6.29	6.23	0.98	Fe XIV	252.200	0.95
270.52	680	180.7	6.29	6.24	0.91	Fe XIV	270.521	0.96
211.32	659	654.5	6.29	6.24	1.00	Fe XIV	211.317	0.96
284.16	1090	916.4	6.34	6.25	0.89	Fe XV	284.163	0.96

**Table 10.** Same as Table 1, but for a QS off-limb observation on 28 July 2017

$\lambda_{\text{obs}}$	DN	$I_{\text{obs}}$	$\log T_{\text{max}}$	$\log T_{\text{eff}}$	$R$	Ion	$\lambda_{\text{exp}}$	$r$
194.66	278	17.5	5.72	6.05	0.86	Fe VIII	194.661	0.95
185.22	233	59.9	5.73	6.05	1.21	Fe VIII	185.213	0.96
186.60	302	55.5	5.73	6.06	1.02	Fe VIII	186.598	0.86
189.94	571	62.8	5.94	6.09	0.84	Fe IX	189.935	0.96
188.49	850	111.0	5.95	6.09	0.95	Fe IX	188.493	0.89
197.85	933	56.6	5.96	6.09	0.95	Fe IX	197.854	0.94
257.26	893	425.8	6.04	6.11	0.90	Fe X	257.259	0.23
						Fe X	257.263	0.75
177.24	241	1246.1	6.05	6.11	0.96	Fe X	177.240	0.98
174.53	128	2006.8	6.05	6.11	1.06	Fe X	174.531	0.98
184.54	1570	550.6	6.05	6.11	0.81	Fe X	184.537	0.97
190.04	2100	227.9	6.06	6.12	0.81	Fe XII	190.040	0.12
						Fe X	190.037	0.77
192.02	518	41.4	5.74	6.12	0.91	Fe XI	192.021	0.84
184.79	110	34.1	6.11	6.12	1.04	Fe XI	184.793	0.80
						Fe X	184.828	0.14
257.55	254	118.4	6.12	6.13	1.02	Fe XI	257.554	0.70
						Fe XI	257.547	0.26
256.92	379	185.2	6.12	6.13	0.79	Fe XI	256.919	0.92
182.17	451	362.8	6.13	6.13	0.77	Fe XI	182.167	0.97
181.13	93	107.3	6.13	6.13	0.89	Fe XI	181.130	0.97
188.22	6750	917.3	6.13	6.13	1.04	Fe XI	188.216	0.98
188.30	4190	563.3	6.13	6.13	1.04	Fe XI	188.299	0.98
192.81	3440	244.1	5.42	6.13	0.83	Fe XI	192.813	0.96
180.40	1310	1948.3	6.13	6.13	1.02	Fe XI	180.401	0.98
202.71	340	76.6	6.13	6.13	1.06	Fe XI	202.705	0.95
258.37	827	364.7	6.15	6.13	0.90	Si X	258.374	0.97
253.79	118	73.1	6.15	6.13	0.89	Si X	253.790	0.97
271.99	556	160.0	6.15	6.13	0.90	Si X	271.992	0.97
261.06	530	194.3	6.15	6.13	0.89	Si X	261.056	0.98
277.27	288	124.5	6.15	6.13	0.88	Si X	277.264	0.98
256.40	697	353.8	6.16	6.13	0.94	Si X	256.377	0.62
						Fe XII	256.410	0.16
						Fe X	256.398	0.11
249.39	47	46.2	6.19	6.14	1.34	Fe XII	249.388	0.69
						Fe XII	249.384	0.22
196.64	1220	68.3	6.19	6.14	1.00	Fe XII	196.640	0.93
186.88	1480	260.6	6.19	6.15	0.95	Fe XII	186.854	0.17
						Fe XII	186.887	0.78
193.51	11600	707.2	6.19	6.15	1.12	Fe XII	193.509	0.94
192.39	5210	393.8	6.19	6.15	0.92	Fe XII	192.394	0.96
195.12	17700	899.4	6.19	6.15	1.26	Fe XII	195.119	0.97
200.02	683	56.4	6.25	6.16	0.77	Fe XIII	200.021	0.89
196.52	379	20.9	6.24	6.16	0.81	Fe XIII	196.525	0.88
264.79	338	108.4	6.29	6.16	0.90	Fe XIV	264.789	0.57
						Fe XI	264.772	0.40
203.83	527	168.7	6.25	6.16	1.07	Fe XIII	203.795	0.28
						Fe XIII	203.826	0.64
251.95	192	140.7	6.25	6.16	0.94	Fe XIII	251.952	0.97
209.92	92	78.2	6.25	6.16	1.07	Fe XIII	209.916	0.95
204.94	101	44.0	6.25	6.16	0.78	Fe XIII	204.942	0.95
202.04	3060	558.8	6.25	6.16	0.85	Fe XIII	202.044	0.97
274.20	293	91.0	6.29	6.18	0.95	Fe XIV	274.204	0.92
211.32	148	159.7	6.29	6.18	0.93	Fe XIV	211.317	0.95
257.40	65	30.6	6.29	6.18	0.87	Fe XIV	257.394	0.96
270.52	99	30.4	6.29	6.18	1.22	Fe XIV	270.521	0.97
284.16	123	119.6	6.34	6.20	0.89	Fe XV	284.163	0.96

**Table 11.** Same as Table 1, but for a QS off-limb observation on 28 June 2019

$\lambda_{\text{obs}}$	DN	$I_{\text{obs}}$	$\log T_{\text{max}}$	$\log T_{\text{eff}}$	$R$	Ion	$\lambda_{\text{exp}}$	$r$
194.66	417	24.4	5.72	6.07	0.80	Fe VIII	194.661	0.95
185.22	412	99.3	5.73	6.07	0.94	Fe VIII	185.213	0.95
186.60	464	74.8	5.73	6.07	0.99	Fe VIII	186.598	0.83
189.94	785	67.3	5.94	6.09	1.11	Fe IX	189.935	0.97
188.49	1290	170.0	5.95	6.09	0.86	Fe IX	188.493	0.89
197.85	1320	78.0	5.96	6.09	0.96	Fe IX	197.854	0.94
257.26	1510	587.6	6.04	6.11	0.90	Fe X	257.259	0.25
						Fe X	257.263	0.73
177.24	346	1672.1	6.05	6.11	1.02	Fe X	177.240	0.98
174.53	177	2598.2	6.05	6.11	1.16	Fe X	174.531	0.98
184.54	2280	626.5	6.05	6.11	1.02	Fe X	184.537	0.96
190.04	3050	256.1	6.06	6.12	1.05	Fe XII	190.040	0.13
						Fe X	190.037	0.75
184.79	164	42.8	6.12	6.13	1.22	Fe XI	184.793	0.94
257.55	441	169.8	6.12	6.14	1.07	Fe XI	257.554	0.70
						Fe XI	257.547	0.26
256.92	608	241.2	6.12	6.14	0.87	Fe XI	256.919	0.92
189.02	427	48.1	6.13	6.14	0.86	Fe XI	188.997	0.96
182.17	710	534.9	6.13	6.14	0.81	Fe XI	182.167	0.97
181.13	150	163.6	6.13	6.14	0.92	Fe XI	181.130	0.97
188.22	9190	1271.2	6.13	6.14	1.11	Fe XI	188.216	0.97
188.30	6090	834.3	6.13	6.14	1.03	Fe XI	188.299	0.97
192.81	5040	329.8	5.42	6.14	0.91	Fe XI	192.813	0.96
180.40	1820	2525.3	6.13	6.14	1.16	Fe XI	180.401	0.97
202.71	424	87.9	6.13	6.14	1.38	Fe XI	202.705	0.93
258.37	1460	545.1	6.15	6.15	0.98	Si X	258.374	0.97
253.79	223	115.0	6.15	6.15	0.92	Si X	253.790	0.97
271.99	852	226.4	6.15	6.15	0.95	Si X	271.992	0.97
261.06	853	274.5	6.15	6.15	0.94	Si X	261.056	0.98
277.27	452	181.3	6.15	6.15	0.91	Si X	277.264	0.98
256.40	1050	430.4	6.16	6.15	1.20	Si X	256.377	0.60
						Fe XII	256.410	0.17
						Fe X	256.398	0.11
249.39	107	92.1	6.19	6.16	1.12	Fe XII	249.388	0.70
						Fe XII	249.384	0.22
196.64	2360	129.1	6.19	6.16	0.97	Fe XII	196.640	0.94
186.88	3170	480.7	6.19	6.16	0.97	Fe XII	186.854	0.17
						Fe XII	186.887	0.77
193.51	18200	1032.8	6.19	6.17	1.25	Fe XII	193.509	0.94
192.39	8090	569.2	6.19	6.17	1.05	Fe XII	192.394	0.96
195.12	27800	1411.7	6.19	6.17	1.31	Fe XII	195.119	0.97
196.52	751	40.7	6.24	6.19	0.94	Fe XIII	196.525	0.91
200.02	1510	109.3	6.25	6.19	0.90	Fe XIII	200.021	0.94
261.73	92	28.4	6.25	6.19	1.13	Fe XIII	261.743	0.97
203.83	1600	417.7	6.25	6.19	1.04	Fe XIII	203.795	0.28
						Fe XIII	203.826	0.65
251.95	421	269.2	6.25	6.19	1.01	Fe XIII	251.952	0.96
204.94	180	59.0	6.25	6.19	1.18	Fe XIII	204.942	0.96
209.92	135	149.7	6.25	6.19	1.04	Fe XIII	209.916	0.95
202.04	5070	909.0	6.25	6.19	0.98	Fe XIII	202.044	0.96
264.79	858	239.6	6.29	6.19	0.92	Fe XIV	264.789	0.71
						Fe XI	264.772	0.26
274.20	835	238.7	6.29	6.21	0.96	Fe XIV	274.204	0.94
252.20	58	36.4	6.29	6.21	1.10	Fe XIV	252.200	0.94
257.40	180	69.9	6.29	6.21	1.05	Fe XIV	257.394	0.96
211.32	370	418.2	6.29	6.21	0.97	Fe XIV	211.317	0.96
270.52	398	112.4	6.29	6.21	0.91	Fe XIV	270.521	0.96
284.16	445	388.2	6.34	6.23	1.02	Fe XV	284.163	0.96

**Table 12.** Same as Table 1, but for an off-limb observation on 5 April 2020 (active Sun)

$\lambda_{\text{obs}}$	DN	$I_{\text{obs}}$	$\log T_{\text{max}}$	$\log T_{\text{eff}}$	$R$	Ion	$\lambda_{\text{exp}}$	$r$
194.66	1220	71.4	5.72	5.91	0.96	Fe VIII	194.661	0.97
189.94	1140	97.4	5.94	6.06	1.14	Fe IX	189.935	0.97
188.49	1560	205.9	5.95	6.06	1.02	Fe IX	188.493	0.90
197.85	1540	91.2	5.96	6.08	1.05	Fe IX	197.854	0.91
257.26	1400	546.5	6.04	6.12	0.88	Fe X	257.259	0.38
						Fe X	257.263	0.60
186.60	1560	252.8	5.73	6.13	1.11	Ca XIV	186.610	0.17
						Fe VIII	186.598	0.74
174.53	217	3193.6	6.05	6.13	1.08	Fe X	174.531	0.98
177.24	418	2020.2	6.05	6.13	0.97	Fe X	177.240	0.97
185.22	2190	528.3	5.73	6.14	0.80	Ni XVI	185.230	0.26
						Fe VIII	185.213	0.71
184.54	2840	781.1	6.05	6.14	1.02	Fe X	184.537	0.92
190.04	3690	310.4	6.05	6.15	1.22	Fe XII	190.040	0.19
						Fe X	190.037	0.64
184.79	498	129.9	6.12	6.17	1.30	Fe XI	184.793	0.95
257.55	669	257.5	6.12	6.17	1.09	Fe XI	257.554	0.68
						Fe XI	257.547	0.25
192.81	6680	437.5	5.42	6.17	0.95	Fe XI	192.813	0.94
189.02	1250	141.4	6.13	6.18	0.97	Fe XI	188.997	0.96
180.60	202	262.5	6.13	6.18	0.79	Fe XI	180.594	0.96
181.13	263	287.3	6.13	6.18	1.01	Fe XI	181.130	0.96
256.92	613	242.9	6.13	6.18	0.90	Fe XII	256.946	0.11
						Fe XI	256.919	0.86
182.17	1280	964.9	6.13	6.18	0.83	Fe XI	182.167	0.96
188.22	13600	1881.0	6.13	6.18	1.02	Fe XI	188.216	0.97
188.30	8400	1150.7	6.13	6.18	0.99	Fe XI	188.299	0.97
180.40	2720	3787.9	6.13	6.18	1.02	Fe XI	180.401	0.97
271.99	1250	330.8	6.15	6.20	1.00	Si X	271.992	0.97
258.37	2900	1088.4	6.15	6.20	1.03	Si X	258.374	0.97
261.06	1170	374.8	6.15	6.20	1.03	Si X	261.056	0.98
253.79	381	195.6	6.15	6.20	1.14	Si X	253.790	0.97
277.27	573	230.0	6.15	6.20	1.10	Si X	277.264	0.98
249.39	246	211.0	6.19	6.21	1.08	Fe XII	249.388	0.72
						Fe XII	249.384	0.20
256.40	2490	1017.8	6.17	6.22	0.95	Si X	256.377	0.48
						Fe XIII	256.400	0.22
						Fe XII	256.410	0.19
196.64	7500	411.2	6.19	6.22	0.92	Fe XII	196.640	0.94
193.51	36700	2073.0	6.19	6.23	1.19	Fe XII	193.509	0.95
192.39	15800	1110.8	6.20	6.23	1.04	Fe XII	192.394	0.96
195.12	57900	2941.0	6.20	6.23	1.22	Fe XII	195.119	0.97
186.88	11000	1664.6	6.19	6.23	0.93	Fe XII	186.854	0.23
						Fe XII	186.887	0.69
196.52	6670	360.9	6.24	6.27	0.80	Fe XIII	196.525	0.95
261.73	327	100.6	6.24	6.27	1.08	Fe XIII	261.743	0.97
246.21	632	692.5	6.25	6.27	0.84	Fe XIII	246.209	0.94
200.02	7700	555.3	6.25	6.27	1.08	Fe XIII	200.021	0.96
251.95	1780	1131.8	6.25	6.27	0.95	Fe XIII	251.952	0.97
203.83	9910	2591.9	6.25	6.27	1.09	Fe XIII	203.795	0.27
						Fe XIII	203.826	0.69
204.94	684	224.1	6.25	6.27	1.11	Fe XIII	204.942	0.96
209.92	270	300.5	6.25	6.27	1.11	Fe XIII	209.916	0.95
202.04	11600	2080.3	6.25	6.27	0.91	Fe XIII	202.044	0.96
264.79	7330	2033.9	6.29	6.31	0.89	Fe XIV	264.789	0.92
274.20	6900	1978.6	6.29	6.31	0.93	Fe XIV	274.204	0.96
252.20	771	476.8	6.29	6.32	0.88	Fe XIV	252.200	0.96
270.52	3910	1102.0	6.29	6.32	0.83	Fe XIV	270.521	0.97
211.32	3020	3410.9	6.30	6.32	0.99	Fe XIV	211.317	0.97
257.40	1540	595.2	6.29	6.32	1.12	Fe XIV	257.394	0.96
284.16	12800	11211.0	6.34	6.39	1.00	Fe XV	284.163	0.98